Technische Universität München
Prof. Dr.-Ing. Nikolaus Adams

– **Semesterarbeit** –

Quantification of Initial Condition Uncertainty in Shock-Bubble Interaction

Author:
Alexander Avdonin
Registration Number:
3601787

Supervisor:
Dipl.-Ing. Volker Tritschler
Prof. Dr.-Ing. Nikolaus Adams

25. März 2013
Lehrstuhl für Aerodynamik, Technische Universität München

Bestätigung der eigenständigen Arbeit

Ich erkläre hiermit, dass ich diese Arbeit ohne fremde Hilfe angefertigt und nur die in dem Literaturverzeichnis angeführten Quellen und Hilfsmittel benutzt habe.

München, den 25.03.2013 _____

Name:	Alexander Avdonin
Matrikelnummer	3601787

Abstract

This work is dedicated to examine the impact of the initial condition uncertainties in shock-bubble interactions on quantities of interest. The quantities of interest are characteristic points and the size of the mixing region, the total circulation, the total mixing rate and the total molecular mixing fraction. The interaction of a shock wave with a circular heavy-gas region is investigated by two dimensional high-resolution Navier-Stokes simulations. The initial conditions are matched to previous experimental [1] and numerical works [2]. Based on these works three main uncertainty parameters are defined: the Mach number, the initial bubble deformation and the contamination of the circular SF_6 region with acetone. The compressible multi-component flow solver INCA is coupled with the uncertainty analysis tool Dakota. Dakota uses a polynomial chaos expansion method in order to propagate the initial condition uncertainties to the output quantities of interest.

It was found that the relative deviations of the geometrical quantities and of the circulation are smaller than the relative deviations of the total mixing rate and the total molecular mixing fraction. The Mach number has the strongest impact on the position of characteristic points of the mixing region. The variation of the total mixing rate and the total molecular mixing fraction are mostly affected by the variation of the bubble contamination with acetone. The deviation of the circulation is equally strong influenced by the Mach number and the contamination with acetone. Whereas the size of the mixing area depends on all three uncertainty parameters.

Contents

List of Figures

List of Tables

Notation

Latin characters

a	$[m/s]$	speed of sound
c_p	$[\frac{J}{kgK}]$	specific heat capacity at constant pressure
c_v	$[\frac{J}{kgK}]$	specific heat capacity at constant volume
D	$[m]$	diameter of a bubble
D	$[m^2/s]$	mass diffusion coefficient
$d_{downstream}$	$[m]$	downstream width of a spiral
$d_{upstream}$	$[m]$	upstream width of a spiral
E	$[J/m^3]$	total energy
e	$[J/kg]$	specific internal energy of a system
e		eccentricity
l_x	$[m]$	mixing layer length in streamwise direction
l_y	$[m]$	mixing layer length in spanwise direction
M		Mach number
M	$[kg/kmol]$	molar mass
MMF		total molecular mixing fraction
m	$[kg]$	mass
k	$[\frac{W}{mK}]$	thermal conductivity
p	$[Pa]$	pressure
q_c	$[W/m^2]$	conductive heat flux
q_d	$[W/m^2]$	interspecies diffusional heat flux
R		response function
R	$[\frac{J}{kgK}]$	specific gas constant
R_d	$[m]$	radius of a bubble
R_{univ}	$[\frac{J}{kmolK}]$	universal gas constant
r	$[m]$	distance from a bubble origin to a point
T	$[K]$	temperature
TMR	$[m^2/s]$	total mixing rate
t	$[s]$	time
$\boldsymbol{u}$	$[m/s]$	velocity vector

u	$[m/s]$	streamwise velocity
v	$[m/s]$	spanwise velocity
X		mole fraction
x	$[m]$	streamwise coordinate
$x_{centroid}$	$[m]$	x coordinate of SF_6 centroid
$x_{downstream}$	$[m]$	x coordinate of a bubble downstream point
$x_{upstream}$	$[m]$	x coordinate of a bubble upstream point
Y		mass fraction
y	$[m]$	spanwise coordinate
$\triangle x$	$[m]$	grid spacing in x direction
$\triangle y$	$[m]$	grid spacing in y direction

Greek characters

α		coefficient of a multivariate polynomial
Γ	$[m^2/s]$	circulation
γ		ratio of specific heats
$\underline{\boldsymbol{\delta}}$		unit tensor
μ	$[\frac{kg}{ms}]$	dynamic viscosity
μ		mean value
$\boldsymbol{\xi}$		vector of standardized random variables
ξ		standardized random variable
ρ	$[kg/m^3]$	density
Σ		variance
σ		standard deviation
$\underline{\boldsymbol{\tau}}$		viscous stress tensor
ϕ		polar angle
Ψ		multivariate polynomial
ψ		one dimensional orthogonal polynomial
ψ		characteristic variable
ω	$[1/s]$	vorticity

Abbreviations

CFD	computational fluid dynamics
CFL	Courant-Friedrichs-Lewy (condition)
DNS	direct numerical simulation
EOS	equation of state
FWHM	full width at half maximum
HG	heavy gas
KHI	Kelvin-Helmholtz instabilities
LANL	Los Alamos National Laboratory
MMF	molecular mixing fraction
PCE	polynomial chaos expansion
RMI	Richtmyer-Meshkov instability
SBI	shock-bubble interaction
STD	standard deviance
TMR	total mixing rate

1. Introduction

In the present study viscous two dimensional Navier-Stokes simulations of a shock-wave of $M = 1.2$ in air interacting with a heavy-gas bubble of SF_6 and acetone are performed. The experimental investigation of Tomkins et al. [1] serves as a starting point for the study.

The aim of this work is to define uncertain parameters in the shock-bubble interaction and to investigate their impact on the quantities of interest.

For the numerical simulation a compressible multicomponent flow solver with a low-dissipative 6^{th}-order accurate reconstruction scheme [3] is used. The uncertainty parameters are propagated by a polynomial chaos expansion method to the output quantities of interest using the free software Dakota.

In chapter 2 the characteristic instabilities in shock-bubble interaction are discussed. Then the setup of the experiment of Tomkins et al. is described. On its basis the uncertain parameters are defined and their bounds are chosen. The uncertain parameters are the Mach number of the shock wave, the initial bubble deformation and the acetone contamination of the bubble.

Chapter 3 deals with the numerical simulation of the shock-bubble interaction. The simulation is described starting from general information about governing equations ending with detailed information about the numerical setup and definition of the output quantities of interest, which are characteristic points and size of the mixing region, the total circulation, the total mixing rate and the total molecular mixing fraction.

Uncertainty quantification analysis is described in chapter 4. At first the general approach of using the polynomial chaos expansion method is given. Then the functionality of the free software DAKOTA is presented, which was used for the uncertainty quantification.

Results are discussed in chapter 5. At first the grid convergence study is presented, justifying the choice of the grid. The convergence study is followed by the core of the uncertainty quantification, i.e. mean values and standard deviances of output quantities of interest. The impact of each uncertainty parameter on output quantities is discussed separately investigating the single parameter standard deviations. In addition, the behavior of the output quantities around their mean values is discussed

by means of local sensitivity analysis.

The results are followed by the conclusion in chapter 6 and appendix, where additional information is given, how to perform the uncertainty quantification with Dakota.

2. Shock-Bubble Interaction Problem

2.1. Instabilities in Shock-Bubble Interaction

The main reason for instabilities in shock-bubble interaction at early times is the Richtmyer-Meshkov induced mixing, which is a result of the impulsive acceleration of a density inhomogenity. Richtmyer [4] was the first who studied the high-speed mixing problem both analytically und numerically. Later, Meshkov [5] confirmed the predictions of Richtmyer experimentally. The Richtmyer-Meshkov instability is driven by baroclinic vorticity deposition on the material interface. It results from a misalignment of the pressure gradient ∇p associated with the shock-wave and the density gradient $\nabla \rho$ of the density inhomogenity. The baroclinic vorticity is the initial driving force of the instability. At intermediate and late-times the initial Richtmyer-Meshkov instability (RMI) is accompagnied by Kelvin-Helmholtz instabilities (KHI) as a result of the velocity shear across the material interface. If the initial energy input of the shock-wave is sufficient RMI and KHI produce a turbulent mixing zone where large scales are constantly broken down into smaller structures leading to a wide range of scales.

2.2. Experimental Setup

Numerical simulation is based on the SBI experiment of Tomkins et al. [1], where a heavy gas cylinder in air is hit by a shock wave at Mach number of 1.2. The heavy gas consists of SF_6 seeded with acetone which serves as a tracer for producing mass fraction pictures using planar laser-induced fluorescence. The schematic of the experimental setup taken from [1] is shown in Fig. 2.1. Air is released from the pressurized driver section by puncturing a membrane, from which a shock wave forms and interacts with the heavy gas in the test section. In this experiment the heavy gas is in the form of a vertical cylinder, created using a membraneless approach which involves flowing the gas downward through a circular nozzle under gravity. The velocity at the nozzle is chosen such that the cylinder flow is completely steady throughout the test section. Fig. 2.2 from [1] shows the initial mass fraction of a heavy gas. The maximum mass fraction of heavy gas is estimated to $Y_{HG}^{max} = 0.83$

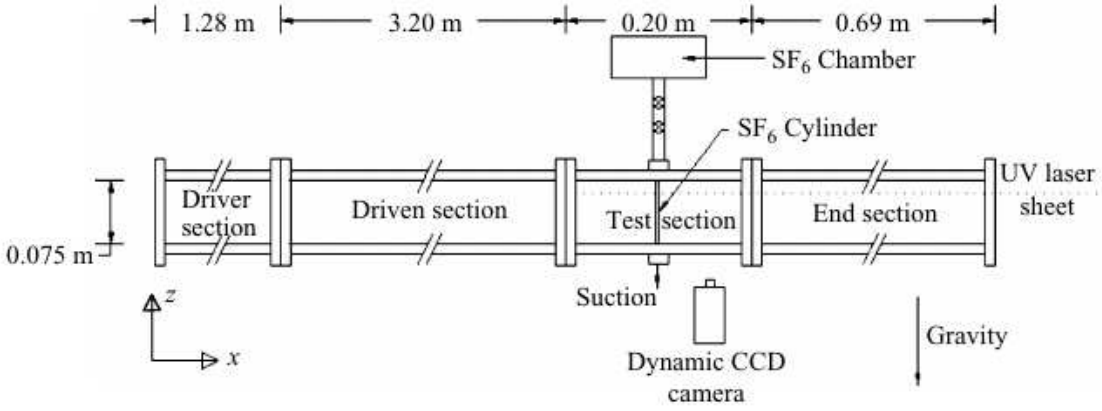

Figure 2.1.: Side-view schematic of LANL shock tube experiment made by Tomkins et al. [1].

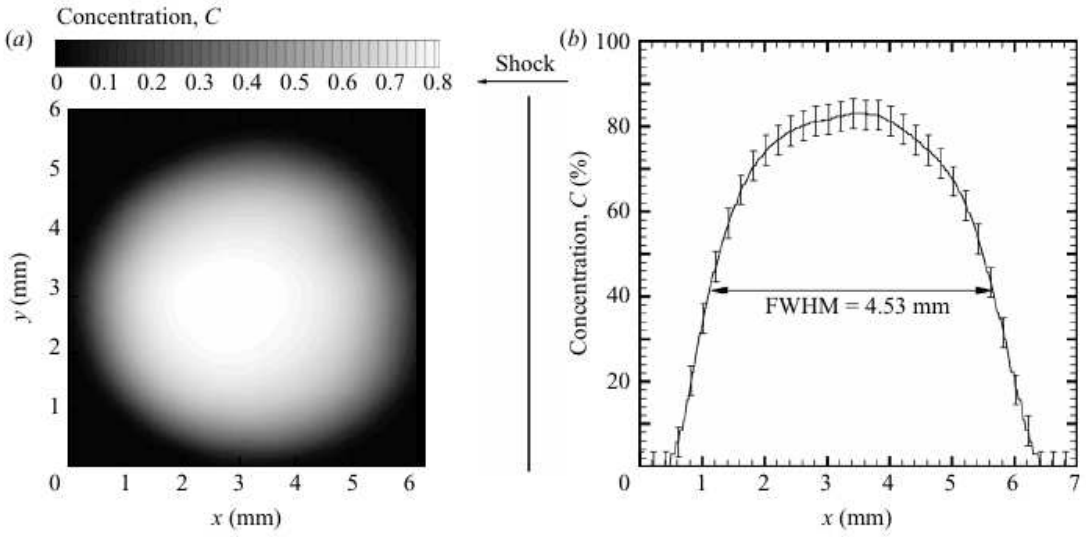

Figure 2.2.: (a) Ensemble-averaged concentration of heavy gas before the shock impact. (b) Lineout through centre of image showing FWHM where error bars are $\pm\sigma$, i.e. one standard deviation in the ensemble. Figure is taken from [1].

with $Y_{HG}^{max} = Y_{Ac}^{max} + Y_{SF6}^{max}$ and $Y_{Air}^{min} = 1 - Y_{HG}^{max} = 0.17$.

2.3. Sources of Uncertainty in Shock-Bubble Interaction

The initial condition of a bubble as well as the strength of the shock wave before it hits a bubble are main sources for the uncertainty in shock-bubble interaction. In this study three uncertain parameters are considered:

1. The Mach number M of a shock wave , as it defines the pressure jump over the shock and accordingly it affects the strength of the RMI. Since the Mach number uncertainty is not given in any paper describing interaction of shock wave with heavy gas bubble, the Mach number uncertainty is assumed to be

$$M \in [1.18, 1.22], \tag{2.3.1}$$

   which is reasonable for this kind of problems. The choice of the uncertainty bounds is based on a private communication with Tomkins et al. and on the Mach number uncertainty from a similar RMI experiment [6].

2. The contamination of the bubble with acetone. It changes the density of the bubble and, as consequence, affects strength of RMI. An uncertainty parameter, maximum mass fraction of acetone in the bubble, Y_{Ac}^{max} is introduced to take the contamination into account. Experimental data on the amount of acetone in the bubble are not available, thus it has to be approximated. Y_{Ac}^{max} is assumed to be

$$Y_{Ac}^{max} \in [0.05, 0.25]. \tag{2.3.2}$$

   Similar values for the acetone concentration can be found in [7],[2] and [8].

3. The bubble deformation is the third important uncertainty parameter since it influences the misalignment of the pressure gradient ∇p and the density gradient $\nabla \rho$. Since the problem is modeled in two dimensions with a symmetry plane in the center of the bubble, only symmetrical deformations can be considered , e.g. stretching/shrinking in streamwise and spanwise directions. To take that into account, the bubble is modeled as an ellipse with the eccentricity e as an uncertainty parameter

$$e \in [-0.5, 0.5], \tag{2.3.3}$$

   where $e > 0$ stretches the bubble in streamwise direction and shrinks it in spanwise direction. $e < 0$ swaps the stretching/shrinking directions. The bubble with $e = -0.5$, $e = 0.0$ and $e = 0.5$ is shown in Fig. 3.5. The choice of this uncertainty parameter is motivated by Fig. 2.2 taken from [1]. It

shows that the cross-section of the heavy gas cylinder in the experiment is not perfectly circular.

More detailed description of uncertainty parameters, such as numerical implementation of their variation, is given in section 4.2.

This study is not focused on reproducing the experiment [1] and its uncertainties, but rather on general effects of possible uncertainties.

3. Shock-Bubble Interaction Simulation

3.1. Governing Equations

The viscous two-dimensional Navier-Stokes equations are solved numerically

$$\frac{\partial \rho}{\partial t} + \nabla \cdot (\rho \boldsymbol{u}) = 0, \tag{3.1.1}$$

$$\frac{\partial (\rho \boldsymbol{u})}{\partial t} + \nabla \cdot (\rho \boldsymbol{u}\boldsymbol{u} + p\underline{\boldsymbol{\delta}} - \underline{\boldsymbol{\tau}}) = 0, \tag{3.1.2}$$

$$\frac{\partial E}{\partial t} + \nabla \cdot [(E+p)\boldsymbol{u}] - \nabla \cdot (\underline{\boldsymbol{\tau}} \cdot \boldsymbol{u} - q_c - q_d) = 0, \tag{3.1.3}$$

$$\frac{\partial \rho Y_i}{\partial t} + \nabla \cdot (\rho \boldsymbol{u} Y_i) - \nabla(\rho D_i \nabla Y_i) = 0. \tag{3.1.4}$$

In system (3.1.1)-(3.1.4) is ρ the mixture density, $\boldsymbol{u}$ is the velocity, p is the pressure, E is the total energy, Y_i is the mass fraction of specie i and $\underline{\boldsymbol{\delta}}$ is the unit tensor. The viscous stress tensor $\underline{\boldsymbol{\tau}}$ is defined for a Newtonian fluid. The heat conduction is defined by $q_c = -\kappa \nabla T$ and q_d defines the interspecies diffusional heat flux according to Cook [9].
The equations are closed with the equation of state (EOS) for an ideal gas

$$p(\rho e, Y_i) = (\overline{\gamma} - 1)\rho e, \tag{3.1.5}$$

where $\overline{\gamma}$ is the ratio of specific heats of the gas mixture. The specific internal energy of the system e is defined as

$$e = \frac{E}{\rho} - \frac{1}{2}\boldsymbol{u}^2. \tag{3.1.6}$$

The specific gas constant of specie i is computed as

$$R_i = \frac{R_{univ}}{M_i}. \tag{3.1.7}$$

The specific heat constants are

$$c_{p,i} = \frac{\gamma_i}{\gamma_i - 1} R_i, \tag{3.1.8}$$

$$c_{v,i} = \frac{1}{\gamma_i - 1} R_i, \tag{3.1.9}$$

where γ_i is the ratio of specific heats of specie i.

3.2. Molecular Mixing Rules

The viscosity coefficient of a pure gas is given by [10]

$$\mu = 2.6693 \cdot 10^{-6} \frac{\sqrt{MT}}{\Omega_\mu \sigma^2}, \tag{3.2.1}$$

where σ is the collision diameter and Ω_μ is the collision integral

$$\Omega_\mu = A(T^*)^B + C \exp\{DT^*\} + E \exp\{FT^*\}, \tag{3.2.2}$$

where $T^* = T/T_\epsilon$ and $A = 1.16145$, $B = -0.14874$, $C = 0.52487$, $D = -0.7732$, $E = 2.16178$ and $F = -2.43787$. $T_\epsilon = \epsilon/k$ is the effective temperature characteristic of the force potential function and k is the Boltzmann constant. The mass diffusion coefficient of a binary mixture can also be calculated from an empirical law given by [11]

$$D_{ij} = \frac{0.0266}{\Omega_D} \frac{T^{3/2}}{p\sqrt{M_{ij}}\sigma_{ij}^2} \tag{3.2.3}$$

with the collision integral for diffusion

$$\Omega_D = A(T^*)^B + C \exp\{DT^*\} + E \exp\{FT^*\} + G \exp\{HT^*\}, \tag{3.2.4}$$

where $A = 1.06036$, $B = -0.1561$, $C = 0.19300$, $D = -0.47635$, $E = 1.03587$, $F = -1.52996$, $G = 1.76474$, $H = -3.89411$ and

$$M_{ij} = \frac{2}{\frac{1}{M_i} + \frac{1}{M_j}}, \tag{3.2.5}$$

$$\sigma_{ij} = \frac{\sigma_i + \sigma_j}{2}, \tag{3.2.6}$$

$$T_\epsilon = \sqrt{\left(\frac{\epsilon}{k}\right)_i \left(\frac{\epsilon}{k}\right)_j}. \tag{3.2.7}$$

The molecular properties of all species in the present study are given in Table 3.1.

Property	Nitrogen	Oxygen	SF_6	Acetone
$(\epsilon/k)_i$	82.0	102.6	212.0	458.0
σ_i	3.738	3.48	5.199	4.599
$M_i[g/mol]$	28.0140	31.9990	146.0570	58.0805
γ_i	1.4	1.4	1.1	1.1

Table 3.1.: Molecular properties of nitrogen, oxygen, SF_6 and acetone.

3.3. Multicomponent Mixing Rules

The ratio of specific heats of the mixture $\overline{\gamma}$ is

$$\overline{\gamma} = \frac{\overline{c_p}}{\overline{c_p} - \overline{R}} \tag{3.3.1}$$

with

$$\overline{c_p} = \sum_i^N Y_i c_{p,i}. \tag{3.3.2}$$

Y_i is the mass fraction of specie i and $\overline{R} = \frac{R_{univ}}{\overline{M}}$ is the specific gas constant of the mixture. The molar mass of the mixture $\overline{M}$ is given by

$$\overline{M} = \left(\sum_i^N \frac{Y_i}{M_i}\right)^{-1}. \tag{3.3.3}$$

The viscosity μ and the heat conductivity coefficient κ of the mixture is calculated from [11]

$$\overline{\chi} = \frac{\sum_{i=1}^{N} \chi Y_i / M_i^{1/2}}{\sum_{i=1}^{N} Y_i / M_i^{1/2}} \tag{3.3.4}$$

with $\chi = \mu, \kappa$. The effective binary diffusion coefficient (diffusion of specie i into all other species) can approximately be calculated by [12]

$$D_i = (1 - X_i) \left(\sum_{i \neq j}^{N} \frac{X_j}{D_{ij}} \right)^{-1} . \tag{3.3.5}$$

X_i is the mole fraction of specie i. Eq. (3.3.5) ensures that the total diffusion flux balance equals zero.

3.4. Numerical Approach

The compressible multi-component flow solver INCA is used to perform CFD simulations. The variables are reconstructed from cell averaged values with the low-dissipative central-upwind 6^{th}-order WENO scheme (WENO-CU6) of Hu et al. [3]. The time derivative is discretized by a third-order total variation diminishing Runge-Kutta scheme, where the time step is determined by the CFL requirement with a CFL number of 0.9.

3.5. Numerical Setup

As already mentioned SBI is studied as two dimensional problem with a symmetry plane through the center of the bubble. Fig. 3.1 shows the simulation domain for SBI. A convective boundary condition[1] is imposed on the left boundary, symmetry on the bottom boundary and outflow on the right and top boundaries. All Simulations are run with CFL number equal to 0.9. The bubble is initialized in the fine grid domain with $\triangle x/D = \triangle y/D = 1.25 \cdot 10^{-5}$, i.e. 480 cells per bubble diameter D. In the coarse grid domain hyperbolic stretching[2] is applied towards the boundaries to reduce the overall number of cells. To reduce the fine grid domain the moving reference frame is introduced. Consequently the pre-shock and post-shock velocities have to be adjusted such that the Mach number of the shock wave in the moving reference frame corresponds to the desired value. The system is Galilean invariant,

[1] for further information, see INCA documentation.
[2] stretching factor $\delta \leq 1.0$.

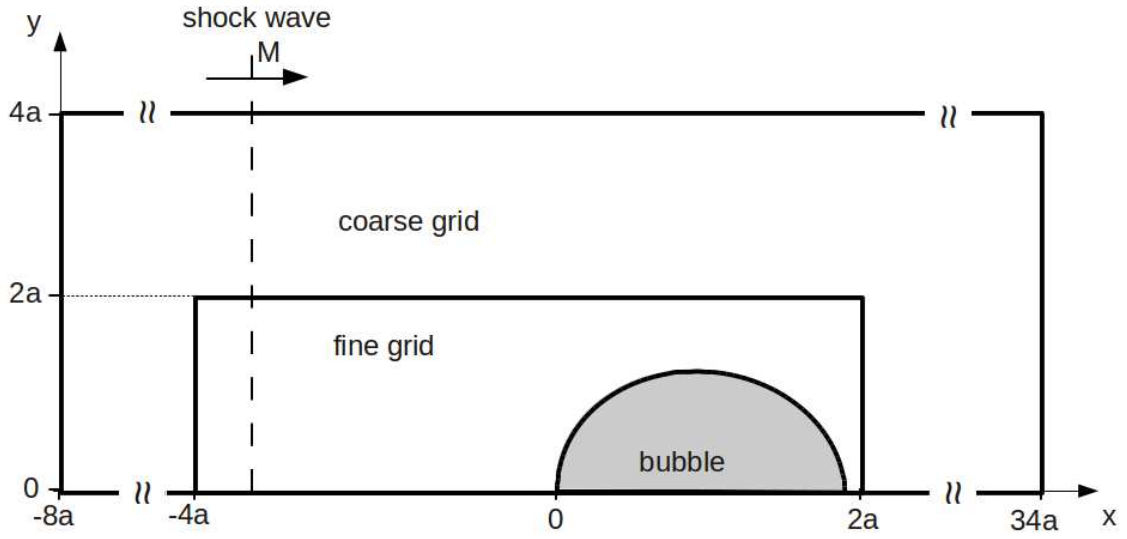

Figure 3.1.: Schematic of the computational domain for the shock bubble interaction. The maximum major axis a equals 3.2 mm.

but in under-resolved simulations a Galilean transformation affects the time evolution of field quantities because of the upwind integration in time. Nevertheless the moving reference frame has to be introduced to reduce drastically the fine grid domain. The simulation without the moving reference frame requires more than 3.5 times longer domain size than with it. To initialize the shock wave with $M = 1.2$, Rankine-Hugoniot conditions are used

$$p_2 = \frac{p_1}{\gamma_{air}+1}(2\gamma_{air}M^2 - (\gamma_{air}-1)), \tag{3.5.1}$$

$$T_2 = T_1 \frac{(1+\frac{\gamma_{air}-1}{2}M^2)(\frac{2\gamma_{air}}{\gamma_{air}-1}M^2 - 1)}{M^2(\frac{2\gamma_{air}}{\gamma_{air}-1} + \frac{\gamma_{air}-1}{2})}, \tag{3.5.2}$$

$$\rho_2 = \frac{p_2}{T_2 R_{air}}, \tag{3.5.3}$$

$$M_2 = \sqrt{\frac{M^2(\gamma_{air}-1)+2}{2\gamma_{air}M^2 - (\gamma_{air}-1)}}, \tag{3.5.4}$$

$$u_2 = M_2\sqrt{\gamma_{air}R_{air}T_2}, \tag{3.5.5}$$

$$\tag{3.5.6}$$

where index "1" belongs to pre-shock quantities $p_1 = 81060\ Pa$, $T_1 = 298\ K$ and $u_1 = 0\ m/s$. Index "2" belongs to post-shock quantities (see Fig. 3.2).

In the case of the moving reference frame the pre-shock and post shock velocities

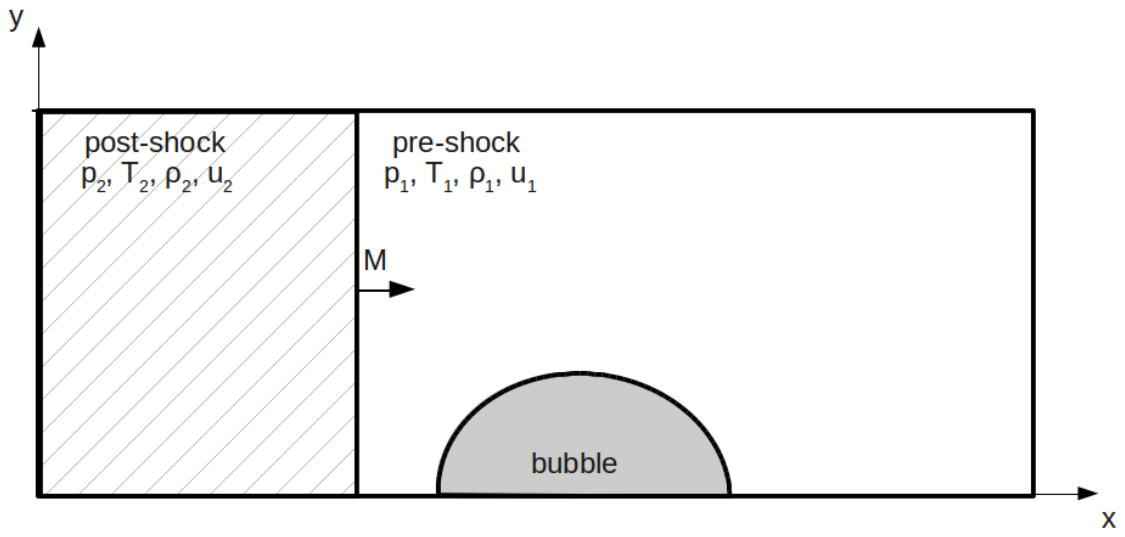

Figure 3.2.: Illustration of pre-shock and post-shock domains.

are superimposed with the frame velocity:

$$u_1 = -u_{frame}, \tag{3.5.7}$$

$$u_2 = -u_{frame} + M_2\sqrt{\gamma_{air}R_{air}T_2}. \tag{3.5.8}$$

u_{frame} is chosen such that bubble remains within the fine grid domain during the simulation time of 640 μs. Since the Mach number of the shock wave varies in this study, an analytical expression for u_{frame} is needed to account for this variation. u_{frame} is calculated using the method of characteristics applied on linearized one dimensional Euler equations [13]. Linearized one dimensional Euler Equations have two characteristic variables

$$\psi_1 = p - \rho_{ref}a_{ref}u, \tag{3.5.9}$$

$$\psi_2 = p + \rho_{ref}a_{ref}u \tag{3.5.10}$$

which are constant along the characteristic equations

$$\left(\frac{dx}{dt}\right)_1 = -a_{ref} + u_{ref}, \tag{3.5.11}$$

$$\left(\frac{dx}{dt}\right)_2 = a_{ref} + u_{ref}. \tag{3.5.12}$$

$$\tag{3.5.13}$$

Fig. 3.3 shows one dimensional interaction of the initial shock wave with the bubble. When the initial shock wave hits the interface, it results in transmission and

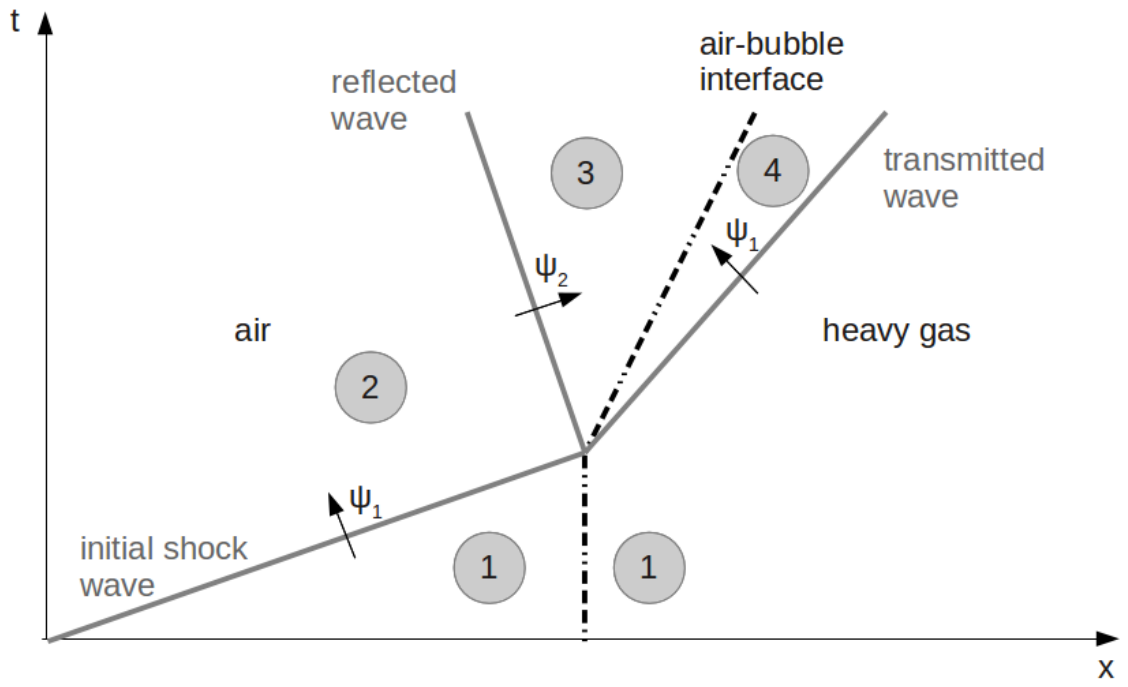

Figure 3.3.: Wave diagram (x-t diagram) of one dimensional shock-bubble interaction.

reflection of the wave. Eq. (3.5.9) - Eq. (3.5.12) with the boundary condition at the interface $u_3 = u_4$ and $p_3 = p_4$ are used to compute the velocity in state 4

$$u_4 = \frac{p_2 + \rho_{2,air} a_{2,air} u_2 - p_1}{\rho_{1,bubble} a_{1,bubble} + \rho_{2,air} a_{2,air}}, \tag{3.5.14}$$

where p_1 is given; p_2, u_2, $a_{2,air}$ and $\rho_{2,air}$ are calculated using Eq. (3.5.1), (3.5.5) and (3.5.3).

$$\rho_{1,bubble} a_{1,bubble} = p_1 T_1 \sqrt{\frac{c_{p,bubble}}{R_{bubble}(c_{p,bubble} - R_{bubble})}}, \tag{3.5.15}$$

$$c_{p,bubble} = \bar{Y}_{Ac} c_{p,Ac} + \bar{Y}_{SF6} c_{p,SF6} + \bar{Y}_{Air} c_{p,Air}, \tag{3.5.16}$$

$$R_{bubble} = R_{univ} \left(\frac{\bar{Y}_{Air}}{M_{Air}} + \frac{\bar{Y}_{Ac}}{M_{Ac}} \frac{\bar{Y}_{SF6}}{M_{SF6}} \right), \tag{3.5.17}$$

where $\bar{Y}_{SF_6}$, $\bar{Y}_{Ac}$ and $\bar{Y}_{air}$ are approximated as one dimensional average over r

$$\bar{Y}_i = \frac{2}{D} \int_0^{D/2} Y_i(r) dr, \tag{3.5.18}$$

where $Y_i(r)$ is given in Eq. (3.5.21) - (3.5.23). The frame velocity is modeled as

$$u_{frame} = 1.12 u_4. \tag{3.5.19}$$

Eq. (3.5.19) is an approximation in order to keep the bubble within the fine grid domain during 640 μs for all variations of uncertainty parameters. If the simulation time has to be extended it is not sufficient to develop a more sophisticated model for u_{frame} since the bubble slightly accelerates due to non linear effects. Therefore the fine grid domain should be extended.

The bubble is initialized with the upstream point fixed at $x/D = -0.5$ (see Fig. 3.1). The shock wave is initialized such that it hits the moving bubble in 12 μs after the initialization.

To model the variation of SF_6 and acetone concentrations within the bubble Eq. from [7] is taken and adopted to this study:

$$Y_{HG}(r) = \begin{cases} Y_{HG,max}\left(1 - \exp\left(\frac{-|\left(\frac{|r|}{R_d}-1\right)\pi|^{1.54}}{1.0082}\right)\right) & if\ |r| \leq R_d \\ 0 & else, \end{cases} \tag{3.5.20}$$

where R_d is the radius of the bubble, $r = \sqrt{(x-x_0)^2 + (y-y_0)^2}$ is the distance to a point (x, y) from the bubble origin (x_0, y_0) $Y_{HG,max}$ is kept constant and equals 0.83. Thus

$$Y_{Air}(r) = 1 - Y_{HG}(r), \tag{3.5.21}$$
$$Y_{Ac}(r) = Y_{Ac}^{max} Y_{HG}(r), \tag{3.5.22}$$
$$Y_{SF6}(r) = (1 - Y_{Ac}^{max}) Y_{HG}(r), \tag{3.5.23}$$
$$\tag{3.5.24}$$

where Y_{Ac}^{max} is given in Eq. (2.3.2). Variation of mole and mass fractions of SF_6 in the bubble is shown in Fig. 3.4. Since SF_6 is heavier than acetone $\frac{\rho_{SF_6}}{\rho_{Ac}} = \frac{M_{SF_6}}{M_{Ac}} \approx 2.5$, their mixing ratio strongly affects the density of the bubble (its value as well as its gradient), which is shown in Fig. 3.5.

The third uncertainty parameter is the eccentricity e. To take into account the bubble deformation, R_d in Eq. (3.5.20) has to be modified. R_d is constant in the case of circle, but if the bubble has an elliptical shape the radius becomes

$$R_d = a = \frac{b}{\sqrt{1 - e^2 \cos^2 \phi}}, \tag{3.5.25}$$

where a is the major semi-axis, b is the minor semi-axis, ϕ is the polar angle. Stretching of the bubble in the x or y direction depends on sign of the eccentricity e. The deformed bubble should have the same area as the circular bubble with $D = 0.006\ m$, thus the relation between a and b is given by

$$a = \frac{D^2}{4a}. \tag{3.5.26}$$

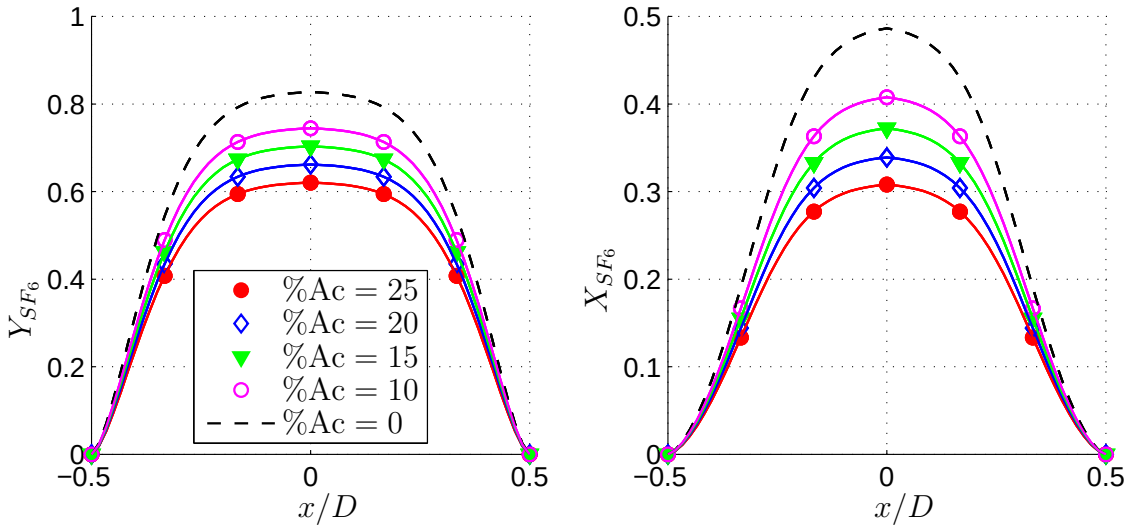

Figure 3.4.: Mass fraction (left) and mole fraction (right) of SF_6 in the bubble with different acetone concentrations.

If $e > 0$ the major axis coincides with x axis and $\cos^2\phi = \frac{(x-x_0)^2}{(x-x_0)^2+(y-y_0)^2}$, where x_0 and y_0 are coordinates of the bubble origin.

If $e < 0$ the major axis is parallel to y axis and $\cos^2\phi = \frac{(y-y_0)^2}{(x-x_0)^2+(y-y_0)^2}$.

If $e = 0$ the ellipse reduces to a circle of constant radius $R_d = D/2$.

All three cases are shown in Fig. 3.5.

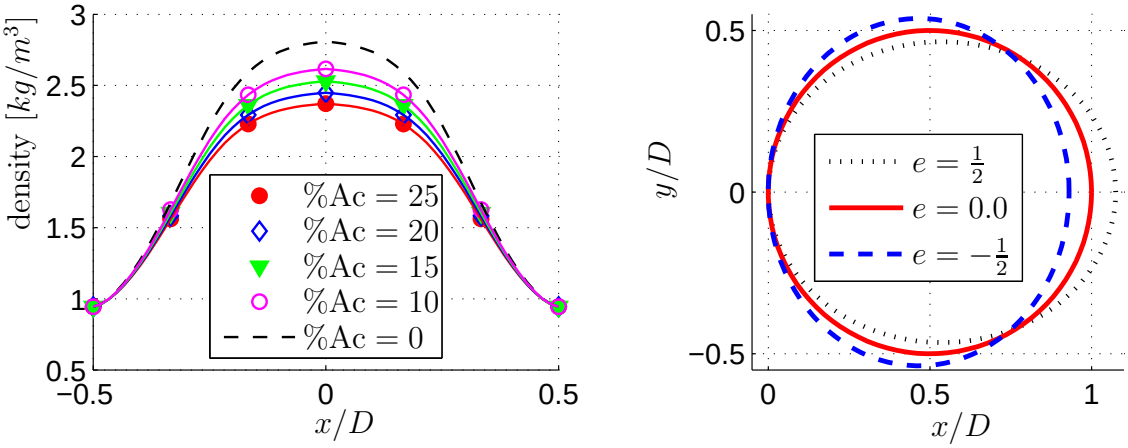

Figure 3.5.: Density of the bubble with different acetone concentrations (left). Shape of the bubble with different eccentricities e (right), the upwind point of all bubble shapes is fixed to the origin.

3.6. Definition of Output Quantities of Interest

To compare the influence of the uncertain parameters the following quantities were chosen as output:

1. Geometrical quantities such as x coordinates of the downstream point $x_{downstream}$, upstream point $x_{upstream}$, centroid of SF_6 $x_{centroid}$, mixing layer length in streamwise direction l_x and spanwise direction l_y, downstream width of the spiral $d_{downstream}$ and upstream width of the spiral $d_{upstream}$. These quantities are shown in Fig. 3.6. $x_{downstream}$ and $x_{upstream}$ are found when the SF_6 mass

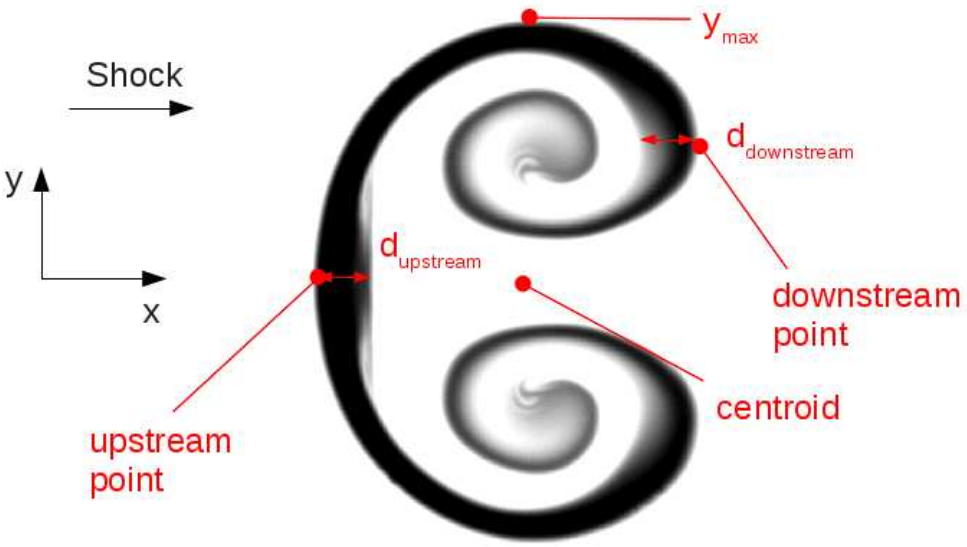

Figure 3.6.: Geometrical quantities.

fraction passes value $0.01max(Y_{SF_6})$. The x coordinate of the centroid of SF_6 is calculated as

$$x_{centroid}^{SF_6} = \frac{\int xY_{SF_6}dxdy}{\int Y_{SF_6}dxdy}. \tag{3.6.1}$$

The mixing layer lengths are computed as

$$l_x = x_{downstream} - x_{upstream}, \tag{3.6.2}$$
$$l_y = 2y_{max}, \tag{3.6.3}$$

where y_{max} is y coordinate of the upper point with SF_6 concentration equals $0.01max(Y_{SF_6})$. Downstream and upstream widths of the spiral are not interesting on its own but their ratio $\frac{d_{downstream}}{d_{upstream}}$ is, since it can be easily compared to the ratio computed from experimental pictures. This quantity has a physical meaning only when the bubble has changed into a system of vortices and the mixing interface has a clear spiral form, which is not strongly distorted.

2. Field quantities such as the circulation Γ which is the integral of the vorticity ω_z over the control volume

$$\Gamma = |\int \omega_z dxdy| = |\int \left(\frac{\partial v}{\partial x} - \frac{\partial u}{\partial y}\right) dxdy|. \tag{3.6.4}$$

Γ is computed only for one half of the heavy gas bubble. The total mixing rate (TMR) is calculated from the gradient of the mass fraction of SF_6. The total mixing rate is defined as the area integral of the scalar mixing rate of SF_6

$$\text{TMR} = \int D_{SF_6} \nabla Y_{SF_6} \cdot \nabla Y_{SF_6} dxdy, \tag{3.6.5}$$

where D_{SF_6} is the effective binary diffusion coefficient of SF_6 into all other species (see Eq. (3.3.5)) The total molecular mixing fraction (MMF) is defined as

$$\text{MMF} = \frac{\int \langle X_{air} X_{HG} \rangle dx}{\int \langle X_{air} \rangle \langle X_{HG} \rangle dx}. \tag{3.6.6}$$

$\langle . \rangle$ indicates spacial averaging in the spanwise direction of the volume fractions X_i. When MMF $= 0$, the two fluids are completely segregated and when MMF $= 1$, they are completely mixed.

To reduce the computational time all integral quantities such as Γ, TMR and MMF are computed for a small box which encloses the bubble. The box boarders are defined by $x_{upstream}$, $x_{downstream}$, $y = 0$ and y_{max}. Since the bubble is growing after the shock impact, the box is growing too. This fact doesn't affect TMR and Γ since ∇Y_{SF_6} is zero and ω_z is negligible outside of the box with the bubble. Nevertheless MMF is affected by the size of the box.

The time evolution of all output parameters starts when the bubble is hit by the shock wave, i.e. the time of the shock impact is set to 0 μs. Geometrical quantities which depend on a frame, e.g. $x_{upstream}$, $x_{centroid}$, $x_{downstream}$, are transformed back to a non-moving reference frame.

4. Uncertainty Quantification Analysis

A brief introduction into uncertainty quantification is given here, which is based on [14]. The goal of the uncertainty quantification method is to determine the uncertainty of outputs (response functions) given the uncertainty of input parameters. The uncertainty quantification analysis is performed with the free software Dakota. As mentioned in section 2.3, three independent uncertainty parameters are chosen for the present study M, e and Y_{SF6}.

4.1. Uncertainty Quantification Methodology

The polynomial chaos expansion (PCE) is a general framework for the approximate representation of random response functions R in terms of finite-dimensional series expansions in standardized random variables $\boldsymbol{\xi} = [\xi_1, \xi_2, ...]$

$$R = \sum_{i=0}^{\infty} \alpha_i \Psi_i(\boldsymbol{\xi}). \tag{4.1.1}$$

In practice, one truncates the infinite expansion at a finite number of random variables and a finite expansion order

$$R \cong \sum_{i=0}^{P} \alpha_i \Psi_i(\boldsymbol{\xi}). \tag{4.1.2}$$

Each of $\Psi_i(\boldsymbol{\xi})$ are multivariate polynomials which involve products of the one-dimensional orthogonal polynomials. According to [14] there is an optimal polynomial for each probability distribution of a uncertain input parameter. Since the probability distributions of the input parameters are unknown, it is assumed to be uniform for all of the uncertain parameters. In the case of uniform distribution Dakota uses product of one dimensional Legendre polynomials for $\Psi(\boldsymbol{\xi})$. Explicit representation of Legendre polynomial is given by

$$\psi_n(\xi) = 2^n \sum_{k=0}^{n} \xi^k \binom{n}{k} \binom{(n+k-1)/2}{n}. \tag{4.1.3}$$

The first few Legendre polynomials are

$$\begin{aligned}
\psi_0(\xi) &= 1, \\
\psi_1(\xi) &= \xi, \\
\psi_2(\xi) &= \frac{1}{2}(3x^2 - 1), \\
\psi_3(\xi) &= \frac{1}{2}(5x^3 - 3x), \\
\psi_4(\xi) &= \frac{1}{8}(35x^4 - 30x^2 + 3), \\
\psi_5(\xi) &= \frac{1}{8}(63x^5 - 70x^3 + 15x).
\end{aligned}$$

The polynomial chaos expansion can include a complete basis of polynomials up to a fixed total-order specification, then expansion orders of one dimensional basis polynomals t_i are constrained by the total expansion order p

$$\sum_{k=1}^{n} t_i \leq p, \tag{4.1.4}$$

where n is a number of random variables. Another possible approach is to employ a tensor-product expansion, in which polynomial order bounds are applied on a per-dimension basis

$$t_i \leq p_i. \tag{4.1.5}$$

The tensor-product expansion supports anisotropy in polynomial order for each dimension, since the polynomial order bounds for each dimension can be specified independently. The total number of terms N_t in an expansion of single orders p_i involving n random variables is given by

$$N_t = 1 + P = \prod_{i=1}^{n}(p_i + 1), \tag{4.1.6}$$

where P comes from Eq. (4.1.2). The multidimensional basis polynomials for a second-order tensor product expansion ($p_1 = 2, p_2 = 2$) over two random dimensions

are

$$\begin{aligned}
\Psi_0(\boldsymbol{\xi}) &= \psi_0(\xi_1)\psi_0(\xi_2) = 1,\\
\Psi_1(\boldsymbol{\xi}) &= \psi_1(\xi_1)\psi_0(\xi_2) = \xi_1,\\
\Psi_2(\boldsymbol{\xi}) &= \psi_2(\xi_1)\psi_0(\xi_2) = \frac{1}{2}(3\xi_1^2 - 1),\\
\Psi_3(\boldsymbol{\xi}) &= \psi_0(\xi_1)\psi_1(\xi_2) = \xi_2,\\
\Psi_4(\boldsymbol{\xi}) &= \psi_1(\xi_1)\psi_1(\xi_2) = \xi_1\xi_2,\\
\Psi_5(\boldsymbol{\xi}) &= \psi_2(\xi_1)\psi_1(\xi_2) = \frac{1}{2}(3\xi_1^2 - 1)\xi_2,\\
\Psi_6(\boldsymbol{\xi}) &= \psi_0(\xi_1)\psi_2(\xi_2) = \frac{1}{2}(3\xi_2^2 - 1),\\
\Psi_7(\boldsymbol{\xi}) &= \psi_1(\xi_1)\psi_2(\xi_2) = \frac{1}{2}\xi_1(3\xi_2^2 - 1),\\
\Psi_8(\boldsymbol{\xi}) &= \psi_2(\xi_1)\psi_2(\xi_2) = \frac{1}{4}(3\xi_1^2 - 1)(3\xi_2^2 - 1).
\end{aligned}$$

Since basis polynomials are orthogonal to each other one can compute α_j applying spectral projection on Eq. (4.1.2)

$$\alpha_j = \frac{\langle R, \Psi_j \rangle}{\langle \Psi_j^2 \rangle} = \frac{1}{\langle \Psi_j^2 \rangle} \int_{\Omega} R\Psi_j \rho(\boldsymbol{\xi}) d\boldsymbol{\xi}, \tag{4.1.7}$$

where $\rho(\boldsymbol{\xi}) = \prod_{i=1}^{n} \rho_i(\xi)$ is a joint probability density function. The probability density function of a single random variable in the case of a uniform distribution is $\rho_i^{uniform} = 1/2$. Ω is a domain spanned by $\boldsymbol{\xi}$. Since only discrete values of R and $\boldsymbol{\xi}$ are available, integration of Eq. (4.1.7) has to be performed numerically. In the case of tensor-product expansion and uniform distribution Dakota performs integration with Gauss-Legendre quadrature rule. This quadrature rule with j integration points yields an exact result for polynomials of degree $2j-1$. The highest order of the integrand in Eq. (4.1.7) is $2p = 2\sum_{i=1}^{n} p_i$ (Ψ_j is of order p and R is modeled to be of order p), therefore $p_i + 1$ integration points in each dimension are needed to obtain good accuracy in α_j. The denominator of Eq. (4.1.7) is computed analytically. One can perform nested quadrature with Gauss-Patterson quadrature rules. The advantage is that previous integration points can be used for higher order PCE. Nevertheless, nested integration requires $p_i + 2$ integration points for the same accuracy as in non nested case. Furthermore the number of integration points in one dimension is restricted to 1, 3, 7 ,15, ... The overall number of integration points for three dimensions is shown in Table 4.1. In three dimensional case nested grid does not have advantage over non-nested grid since nestedness is far too expensive in multidimensional cases. Because of the high computation time of each CFD simulation non-nested quadrature of 4th order accuracy in each dimension with 125 integration points is chosen for the investigation of SBI.

order	$2 \times 2 \times 2$	$3 \times 3 \times 3$	$4 \times 4 \times 4$	$5 \times 5 \times 5$	$6 \times 6 \times 6$	$7 \times 7 \times 7$
non-nested grid	8	64	125	216	343	512
nested grid	27	-	-	343	-	-
sparse grid	7	-	-	31	-	111

Table 4.1.: Number of integration points depending on the grid type and the expansion order in three dimensional case.

Mean and variance of polynomial chaos expansions are available in a simple closed form after computation of α_j:

$$\mu = \langle R \rangle \cong \sum_{k=0}^{P} \alpha_k \langle \Psi_k(\boldsymbol{\xi}) \rangle, \tag{4.1.8}$$

$$\Sigma = \langle (R-\mu)^2 \rangle \cong \sum_{k=0}^{P} \sum_{l=0}^{P} \langle \alpha_k \alpha_l \Psi_k(\boldsymbol{\xi}) \Psi_l(\boldsymbol{\xi}) \rangle = \sum_{k=0}^{P} \alpha_k^2 \langle \Psi_k(\boldsymbol{\xi})^2 \rangle, \tag{4.1.9}$$

where $\langle \Psi_k(\boldsymbol{\xi}) \rangle$ and $\langle \Psi_k(\boldsymbol{\xi})^2 \rangle$ are integrated analytically.

Beside computation of analytical moments PCE is used to perform local sensitivity analysis, i.e. derivatives of a response function with respect to expansion variables:

$$\frac{\partial R}{\partial \xi_i} = \sum_{j=0}^{P} \alpha_j \frac{\partial \Psi_j(\boldsymbol{\xi})}{\partial \xi_i}, \tag{4.1.10}$$

where differentiation of Ψ_j is performed analytically. Dakota computes local sensitivities for each response function R_i evaluated at uncertain variable means $\langle \xi_j \rangle$.

4.2. Standardization of Uncertainty Parameters

After bounds of uncertain parameters are set, they have to be standardized. To transform an uncertain parameter x_i to a standardized uncertain parameter ξ_i, the following linear transformation has to be applied

$$\xi_i = \frac{x_i - \mu_i}{\sigma_i}, \tag{4.2.1}$$

where μ_i is a mean value and σ_i is a standard deviance of x_i. For continuous independent uniform distributed parameters

$$\mu_i = \frac{x_{i,max} + x_{i,min}}{2}, \tag{4.2.2}$$

$$\sigma_i = \frac{x_{i,max} - x_{i,min}}{\sqrt{12}}. \tag{4.2.3}$$

After the transformation all standardized variables have mean value equal to 0 and standard deviance equal to 1. Thus all uncertain parameters defined for this study M, e, Y_{Ac} have the same standardized form (but different μ_i and σ_i)

$$M \in [1.18, 1.22] \longrightarrow \xi_M \in [-1.7321, 1.7321], \tag{4.2.4}$$
$$e \in [-0.5, 0.5] \longrightarrow \xi_e \in [-1.7321, 1.7321], \tag{4.2.5}$$
$$Y_{Ac}^{max} \in [0.05, 0.25] \longrightarrow \xi_{Ac} \in [-1.7321, 1.7321]. \tag{4.2.6}$$

Because of the numerical integration of eq.4.1.7 with Gauss-Legendre quadrature rule, $\Psi_i(\boldsymbol{\xi})$ are not evaluated on at the bounds of the uncertainty parameter intervals, but on

$$M_{min}^{num} = 1.181876, \qquad M_{max}^{num} = 1.2181236, \tag{4.2.7}$$
$$e_{min}^{num} = -0.453090, \qquad e_{max}^{num} = 0.453090, \tag{4.2.8}$$
$$(Y_{Ac}^{max})_{min}^{num} = 0.059382, \qquad (Y_{Ac}^{max})_{max}^{num} = 0.240618. \tag{4.2.9}$$

4.3. Realization

Since Dakota is performing a numerical integration of Eq. (4.1.7), it defines integration points, i.e. uncertain parameter values for which CFD simulations have to be performed. Because of high computational time of a CFD Simulation it is not reasonable to let Dakota control CFD simulations. Instead of that, a list of uncertain parameters, required for performing simulations, was extracted from Dakota using a Fortran program given in A.1. After performing the CFD simulations, the latter list was extended with response function values at each simulation time step. Using another Fortran program A.2, Dakota could access required data and compute uncertainties of response functions for each time step separately. Then data was gathered together.

5. Results

5.1. Grid Convergence Study

Before running the uncertainty quantification study, the grid convergence study with the uncertainty parameters $M = 1.2$, $e = 0.0$, $Y_{Ac} = 0.15$ has been performed. The grid resolutions which have been tested are presented in Table 5.1. The size of the

mesh number	$\frac{D}{\triangle x} = \frac{D}{\triangle y}$	number of cells in fine grid	overall number of cells
1	120	49152	50048
2	240	196608	200192
3	480	786432	800768
4	960	3145700	3203072

Table 5.1.: 2-D mesh specification.

simulation domain was kept constant. The output parameters for different grids are shown in Fig. 5.1 and 5.2.

The analysis of the results is performed in section 5.2, here the grid convergence is discussed. The figures show there is a negligible difference in l_x and l_y between the tested mesh types. Difference in $x_{downstream}$, $x_{upstream}$, $x_{centroid}$ can not be seen because of the scaling of y axis, nevertheless it is deduced from the difference in $l_x = x_{downstream} - x_{upstream}$. It is difficult to compare mesh types considering $d_{downstream}/d_{upstream}$, since its time evolution is not smooth enough. However the finer the grid is, the smother $d_{downstream}/d_{upstream}$ is. Mesh 3 yields $d_{downstream}/d_{upstream}$ which is close to the ratio of spiral widths on Mesh 4. The dependence of Γ on the mesh type is negligible. All mesh types yield comparable values of MMF. TMR is an integral of a product of two gradients, therefore it requires well resolved gradients and TMR is mostly affected by the grid resolution. On mesh 1 to mesh 3 the underresolution triggers secondary instabilities, whereas mesh 4 does not have such instabilities. It can be concluded that mesh 4 has DNS resolution. Mesh 3 is able to reproduce TMR evolution on mesh 4 until 400 μs after the shock impact. After that time mesh 3 overpredicts TMR in comparison to mesh 4. Snapshots of SF_6 mass fraction at different times are shown in Fig. 5.3. Instabilities develop on coarser grid earlier than on finer grid. Image of SF_6 mass fraction on mesh 3 is, like TMR evolution, similar to that on mesh 4 until $t = 400$ μs, then the mixing layer

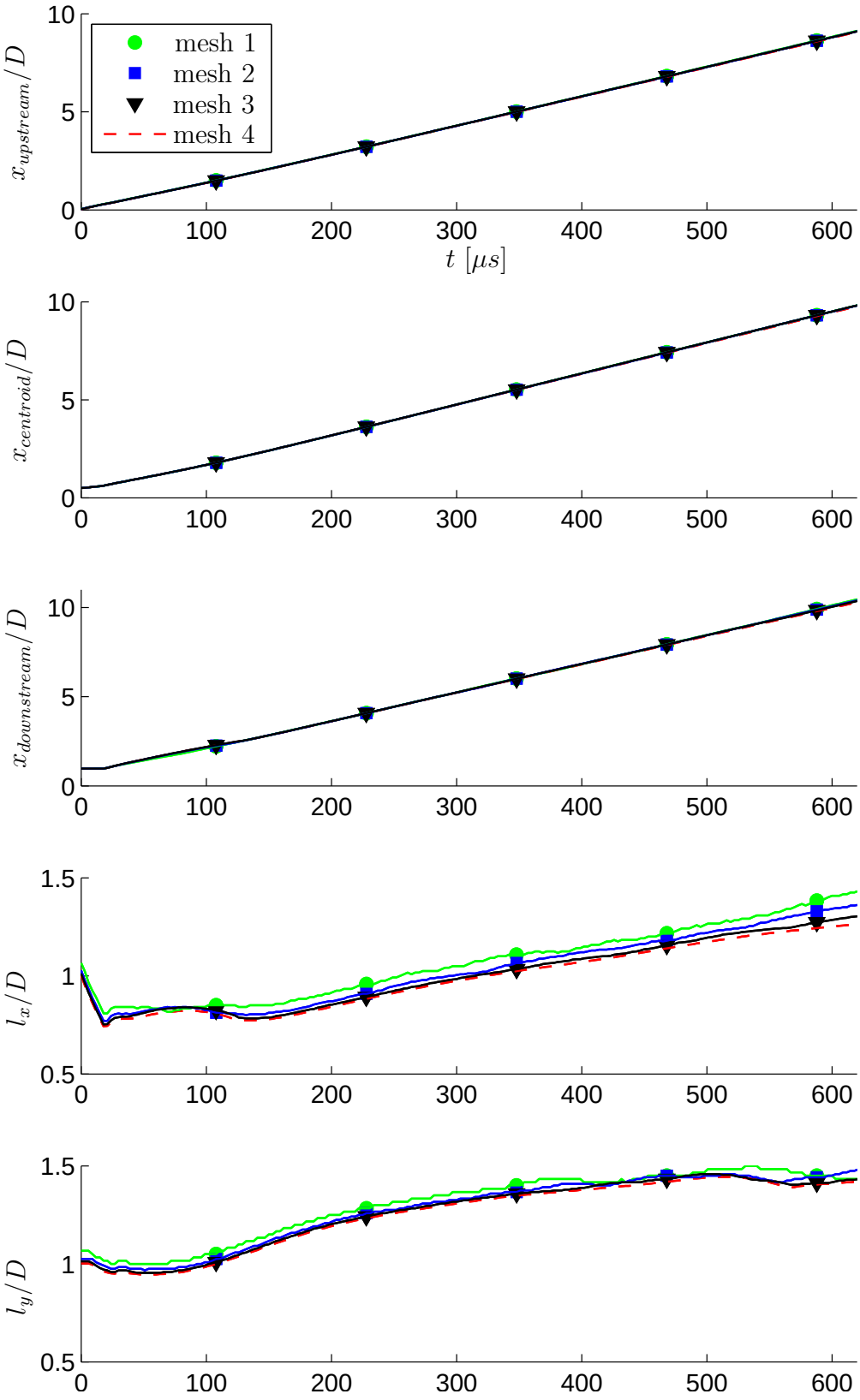

Figure 5.1.: Output parameters for different grid resolutions. Simulations with uncertainty parameters $M = 1.2$, $e = 0.0$, $Y_{Ac} = 0.15$.

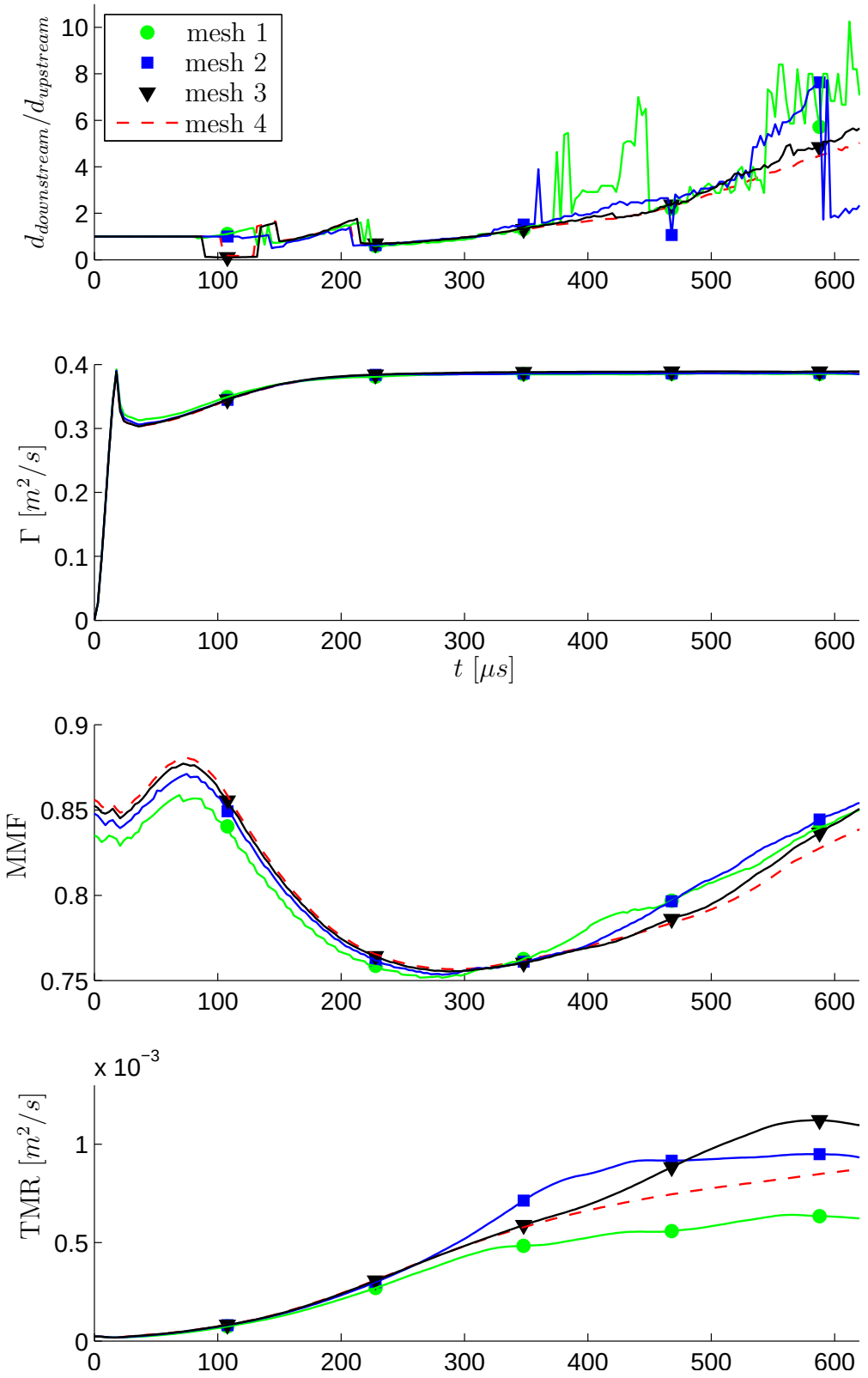

Figure 5.2.: Output parameters for different grid resolutions. Simulations with uncertainty parameters $M = 1.2$, $e = 0.0$, $Y_{Ac} = 0.15$.

becomes unstable.

Mesh 3 yields converged results until $400\mu s$, then it becomes less reliable. Nevertheless it was chosen for the uncertainty quantification study because of the high amount of simulations (125), which have to be performed.

Comparison of experimental and numerical results on the finest grid (see Fig. 5.3) shows that at early times (130 μs) SF_6 mass fraction images are similar. Then the rolling-up process in the numerical simulation occurs faster than in the experiment. That can be concluded from the observation of number of roll-ups in the image. This discrepancy can be explained by the difference in initial conditions between the experiment and the converged simulation on the finest grid. As mentioned earlier, the scope of this study is not to match the experimental results, but to study qualitatively effects of uncertainty parameters. Mesh 3 fulfills the requirements for this study.

5.2. Uncertainty Quantification Results

5.2.1. Mean Value and Standard Deviance

Mean values with standard deviances of output parameters are shown in Fig. 5.4 and 5.5. For all output quantities the mean value almost always coincides with the mean simulation ($e = 0$, $Y_{Ac}^{max} = 0.15$, $M = 1.2$). The evolution of $x_{upstream}$, $x_{centroid}$ and $x_{downstream}$ show approximately linear behavior at late times, i.e. the characteristic points of the bubble are moving with constant velocity. This can be explained by the fact that Γ remains constant at late times. $x_{centroid}$ and $x_{downstream}$ have a constant value until they are hit by a shock wave at $t = 9$ μs and $t = 18$ μs respectively. The deviances from the mean value of $x_{upstream}$, $x_{centroid}$ and $x_{downstream}$ are similar to each over and are slightly growing in time. Standard deviance at latest time achieves the value of $0.5D$.

The bubble contracts until the shock hits the downstream point, i.e. the mixing layer length l_x decreases. After the shock has passed the bubble, it remains contracted until $t = 160$ μs, then it slowly expands in streamwise direction with almost linear growing rate, which is expected since the characteristic points of the bubble move with almost constant speed. The mixing layer length l_y negligibly decreases after the shock impact, then it grows until 500 μs, after that it remains approximately constant. The area with SF_6 is bigger in the end of the simulation than before the shock impact, furthermore it is stretched more in spanwise than in streamwise direction. The standard deviance in both cases is small $\leq 0.05D$. It is not equal to zero at $t = 0$, since e changes the initial shape of the bubble and thus influences directly the standard deviation.

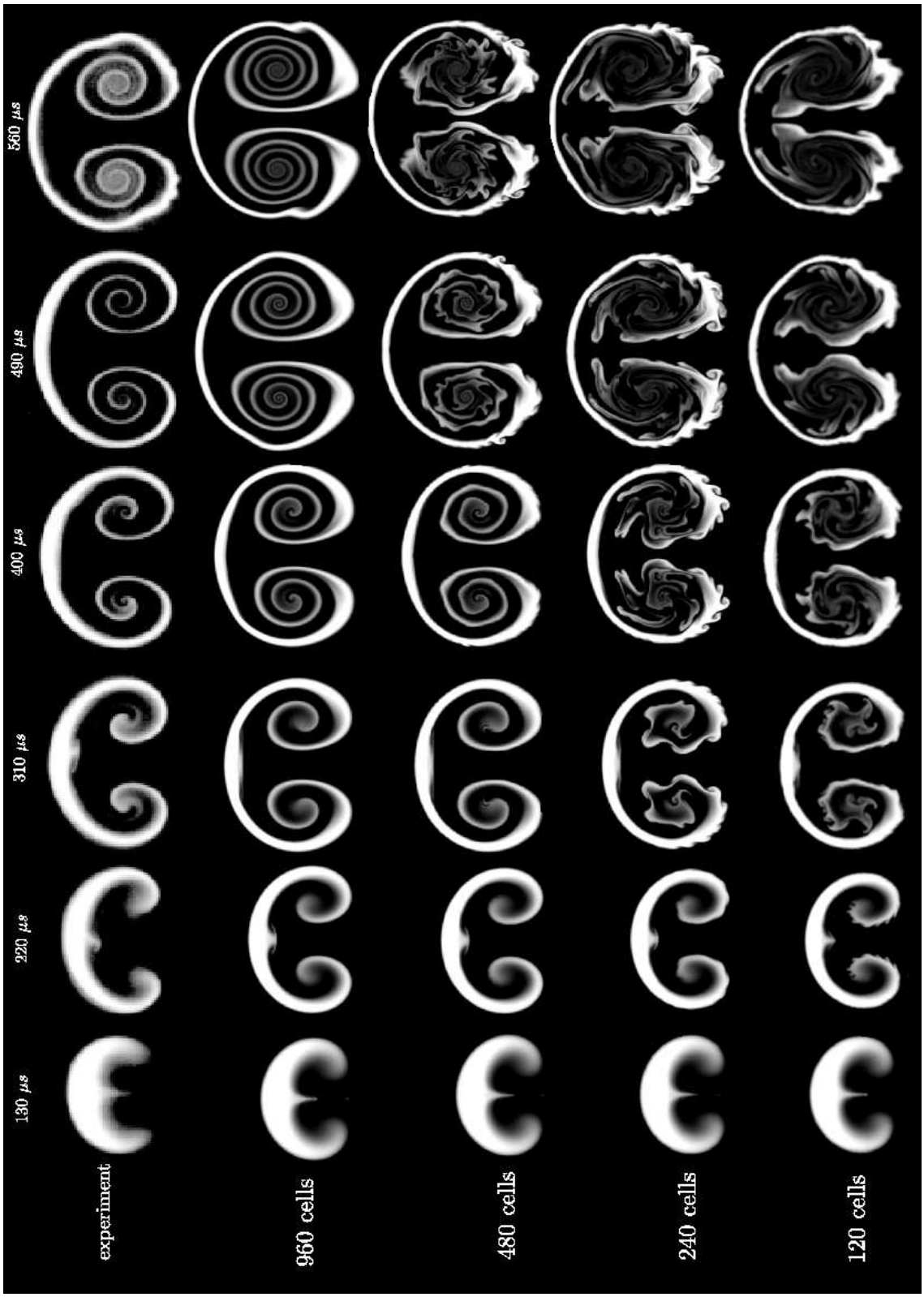

Figure 5.3.: Snapshots of the SF_6 mass fraction in the experiment and in the simulations with different grid resolutions.

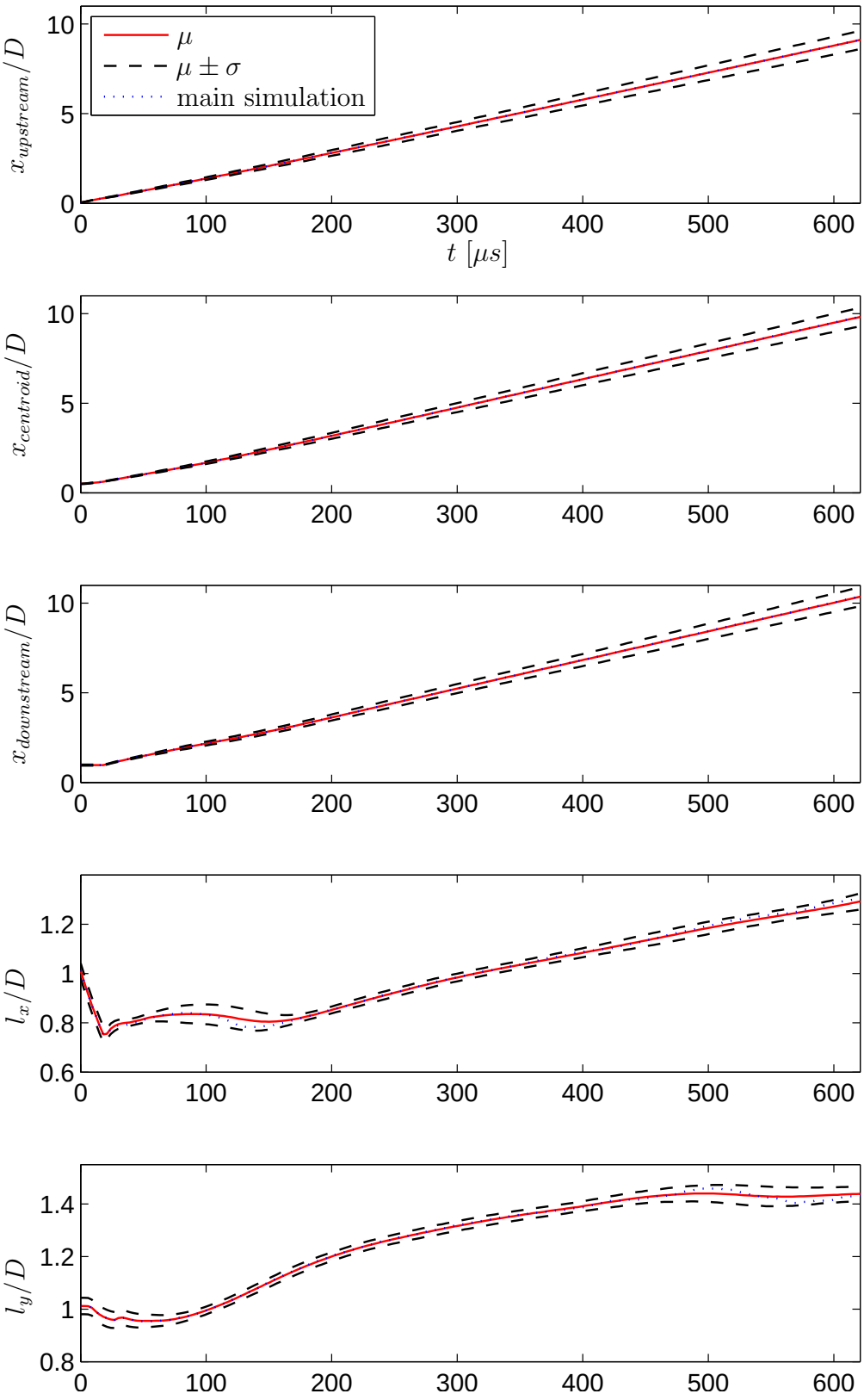

Figure 5.4.: Mean value with standard deviance of output quantities, mean simulation with $e = 0$, $Y_{Ac}^{max} = 0.15$ and $M = 1.2$.

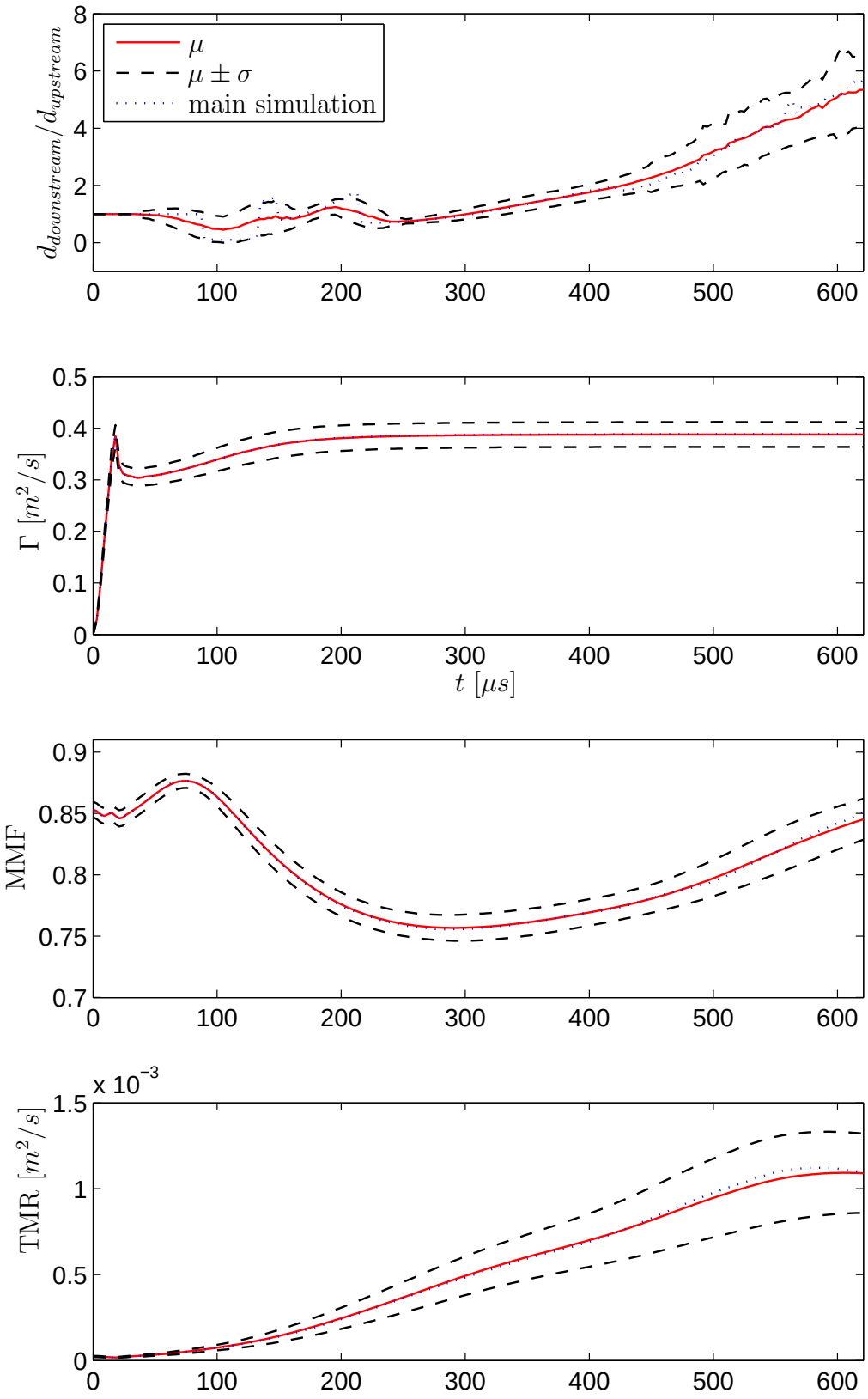

Figure 5.5.: Mean value with standard deviance of output quantities, mean simulation with $e = 0$, $Y_{Ac}^{max} = 0.15$ and $M = 1.2$.

The ratio $\frac{d_{downstream}}{d_{upstream}}$ is around 1 until $t < 300\ \mu s$, then i starts to grow. The standard deviance shows local minimum at $\frac{d_{downstream}}{d_{upstream}}(t = 255\ \mu s) = 0.74$, where σ is almost zero, i.e. at this time $\frac{d_{downstream}}{d_{upstream}}$ is independent from the variation of the input parameters. Therefore $\frac{d_{downstream}}{d_{upstream}}$ should be close to that value from the experiment at the same time. $\frac{d_{downstream}}{d_{upstream}}$ from the experiment of Tomkins et al. at $t = 220\ \mu s$ is estimated to be 0.67 from Fig. 5.3, whereas in the mean simulation $\frac{d_{downstream}}{d_{upstream}} = 0.69$ and the mean value is 0.98.

The total circulation grows linearly as long the shock wave propagates within the bubble. Immediately after the the shock wave has left the bubble Γ decreases. Then it grows again up to the value 0.39 m^2/s and remains constant after that. The same result was obtained in [7]. Even if the viscosity is taken into account in this simulation, the simulation time is too short to see any dissipation of Γ. The standard deviation of Γ is almost zero as long the shock is within the bubble, then it grows up to a constant value 0.024 m^2/s.

MMF grows after the shock has left the bubble, then it starts to fall around $t = 80\ \mu s$. The reason for that is the growing averaging box (l_x and l_y are growing). This effect dominates the mixing process, thus MMF decreases. At $t = 300\ \mu s$ the mixing process becomes stronger than the effect of the growing averaging box, thus MMF increases. The standard deviance of MMF is slightly growing with time and reaches its maximum 0.017 to the end of the simulation.

TMR increases with time indicating stronger mixing process. Its standard deviation increases considerably with time and achieves 20% of the TMR value at the end of the simulation.

One can also plot output parameters of simulations with the highest deviance from the mean value. The outliers, i.e. the simulations with output quantities maximum distant from the mean values averaged over the entire simulation time, are found using the following parameter

$$\langle Z_i \rangle = \frac{1}{n-s} \sum_{j=s}^{n} \frac{R_i(t_j) - \mu_i(t_j)}{\mu_i(t_j)}, \tag{5.2.1}$$

where R_i is the output quantity, μ_i is its mean value, t_j is the time at the time step j, n is the overall number of time steps and s is the offset ($\approx 15\ \mu s$) from the time $t = 0$ to avoid zero values in the denominator of eq.5.2.1. The simulation with the maximum $\langle Z_i \rangle$ is the highest outlier and the simulation with the minimum $\langle Z_i \rangle$ is the lowest outlier. The outliers are shown in Fig. 5.6 and 5.7. In general the output parameters of the highest and lowest outliers are not equidistant to the mean value μ, e.g. the evolution of TMR. Furthermore they do not have to lie always upon or under the mean value, they can switch sides as long the time averaged quantity $\langle Z_i \rangle$ remains maximal or minimal, e.g. the evolution of l_x. The input parameters of the

output parameter	maximum	minimum
$x_{upstream}$	$e = -0.4531$ $Y_{Ac}^{max} = 0.2406$ $M = 1.2181$	$e = 0.4531$ $Y_{Ac}^{max} = 0.0594$ $M = 1.1819$
$x_{centroid}$	$e = -0.4531$ $Y_{Ac}^{max} = 0.2406$ $M = 1.2181$	$e = 0.4531$ $Y_{Ac}^{max} = 0.0594$ $M = 1.1819$
$x_{downstream}$	$e = -0.4531$ $Y_{Ac}^{max} = 0.2406$ $M = 1.2181$	$e = 0.4531$ $Y_{Ac}^{max} = 0.0594$ $M = 1.1819$
l_x	$e = 0.4531$ $Y_{Ac}^{max} = 0.0594$ $M = 1.2181$	$e = 0.4531$ $Y_{Ac}^{max} = 0.2406$ $M = 1.1819$
l_y	$e = -0.4531$ $Y_{Ac}^{max} = 0.0594$ $M = 1.2181$	$e = 0.4531$ $Y_{Ac}^{max} = 0.2406$ $M = 1.1819$
$\frac{d_{downstream}}{d_{upstream}}$	$e = 0.4531$ $Y_{Ac}^{max} = 0.0594$ $M = 1.2181$	$e = -0.4531$ $Y_{Ac}^{max} = 0.2406$ $M = 1.1819$
Γ $[m^2/s]$	$e = 0.4531$ $Y_{Ac}^{max} = 0.0594$ $M = 1.2181$	$e = -0.4531$ $Y_{Ac}^{max} = 0.2406$ $M = 1.1819$
TMR $[m^2/s]$	$e = 0.4531$ $Y_{Ac}^{max} = 0.0594$ $M = 1.2108$	$e = -0.4531$ $Y_{Ac}^{max} = 0.2406$ $M = 1.1819$
MMF	$e = 0.4531$ $Y_{Ac}^{max} = 0.0594$ $M = 1.2181$	$e = -0.4531$ $Y_{Ac}^{max} = 0.2406$ $M = 1.1819$

Table 5.2.: The input parameters of the outliers.

outliers are given in Table 5.2. Almost all outliers have the input parameters at the numerical bounds of the defined intervals (see Eq. (4.2.7) to (2.3.2)).

5.2.2. Single Uncertain Parameter Variation

To decide which uncertainty parameter has the highest influence on the variation of the output parameters, uncertainty quantification analysis was performed for each uncertainty parameter e, M, and Y_{Ac}^{max} separately. Fig. 5.8 and 5.9 show computed standard deviations $\sigma(e)$, $\sigma(M)$, $\sigma(Y_{Ac}^{max})$. Comparison of $\sigma(e)$, $\sigma(M)$ and $\sigma(Y_{Ac}^{max})$ serves to identify importance of the uncertain parameters.

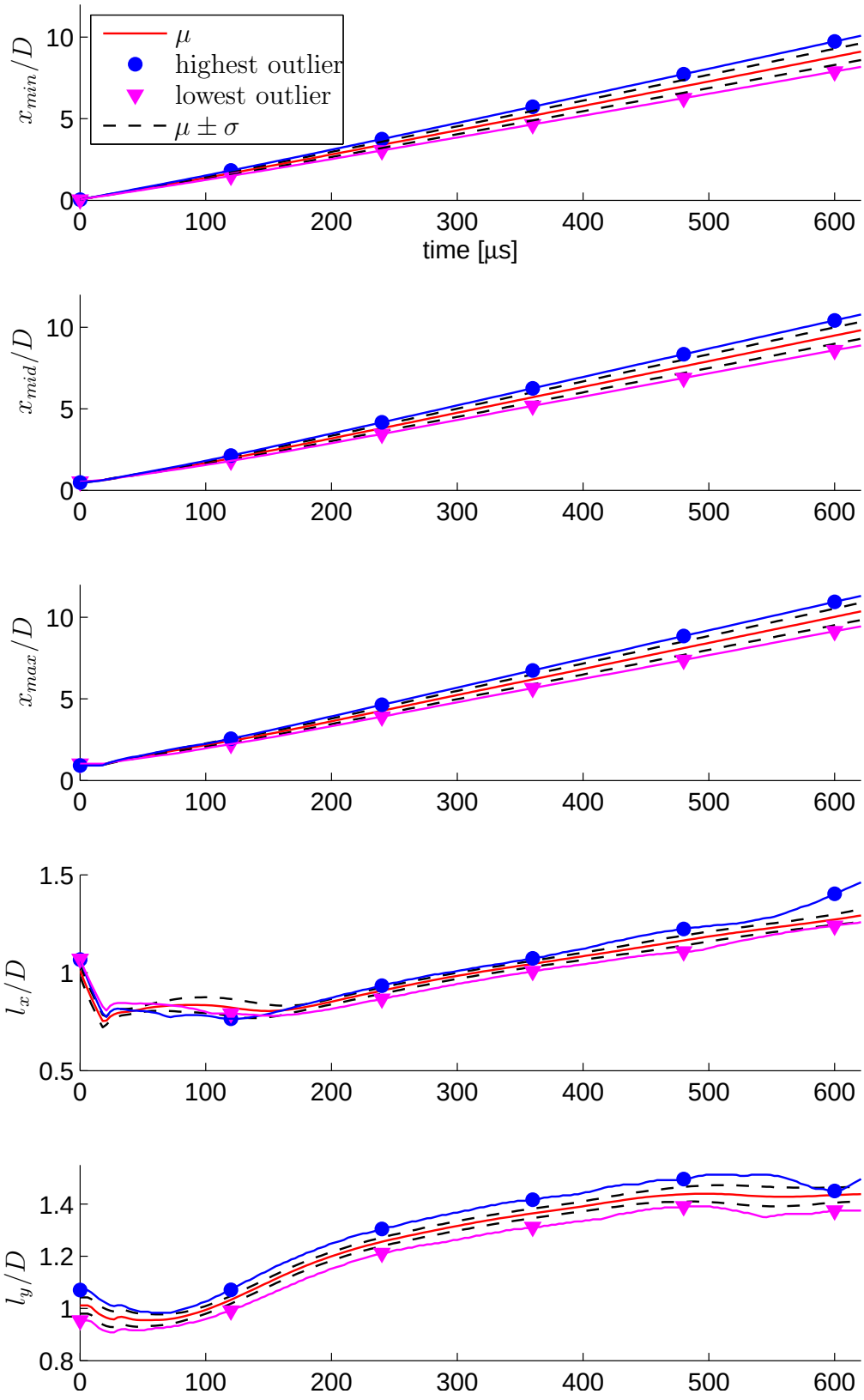

Figure 5.6.: The outliers together with the mean values and standard deviations of the output quantities of interest.

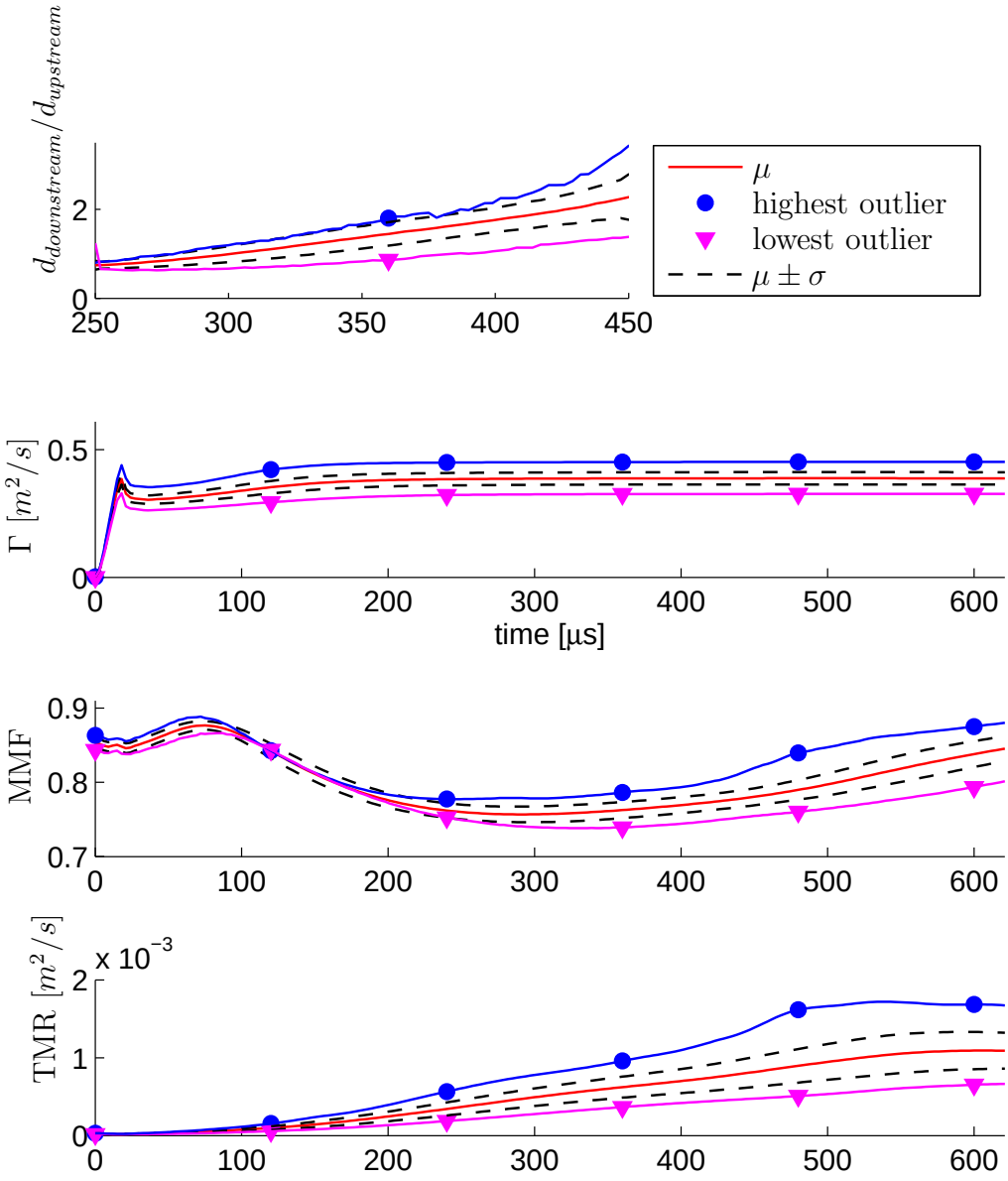

Figure 5.7.: The outliers together with the mean values and standard deviations of the output quantities of interest.

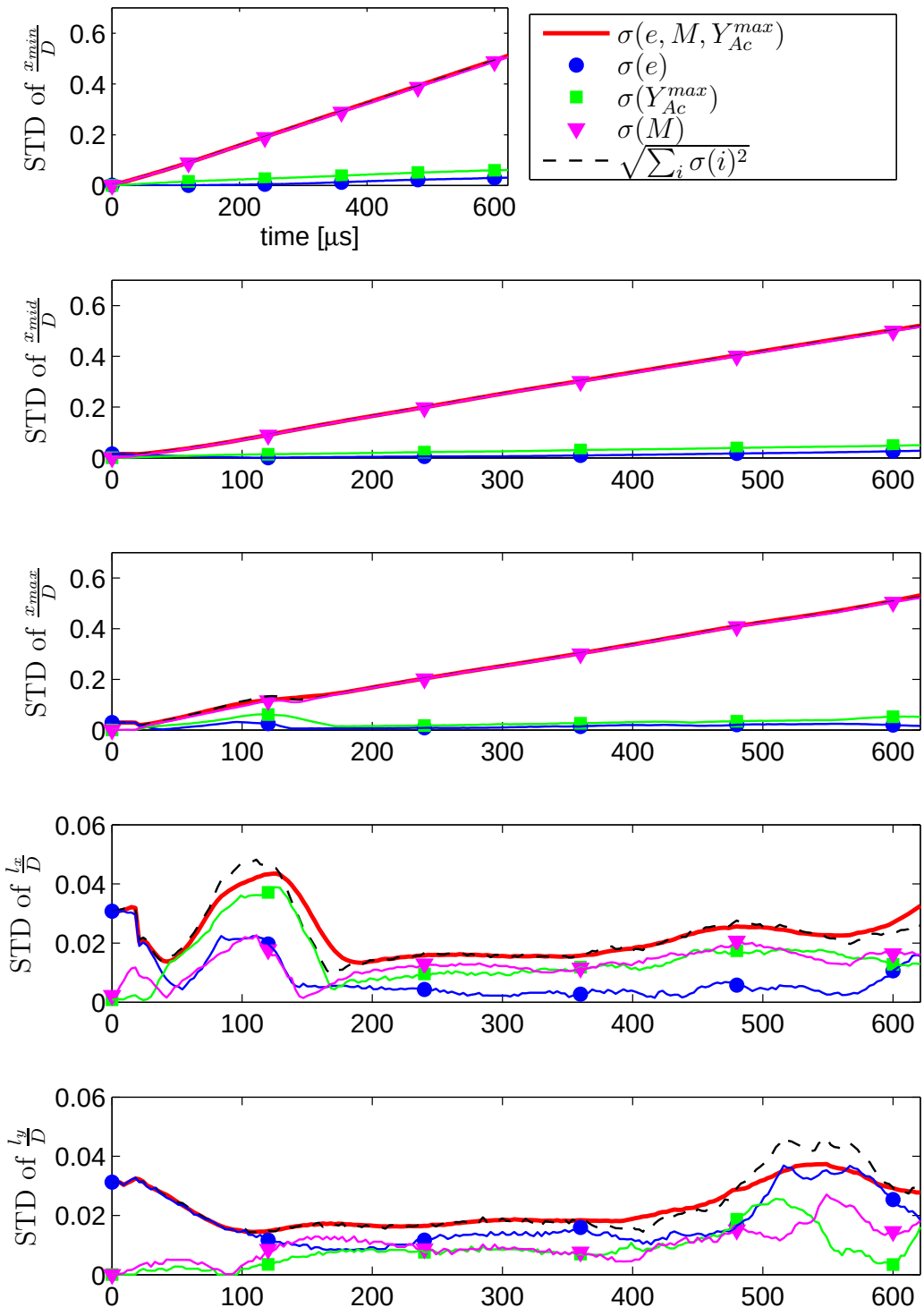

Figure 5.8.: Standard deviations of single uncertain parameter variations and multiple parameter variation.

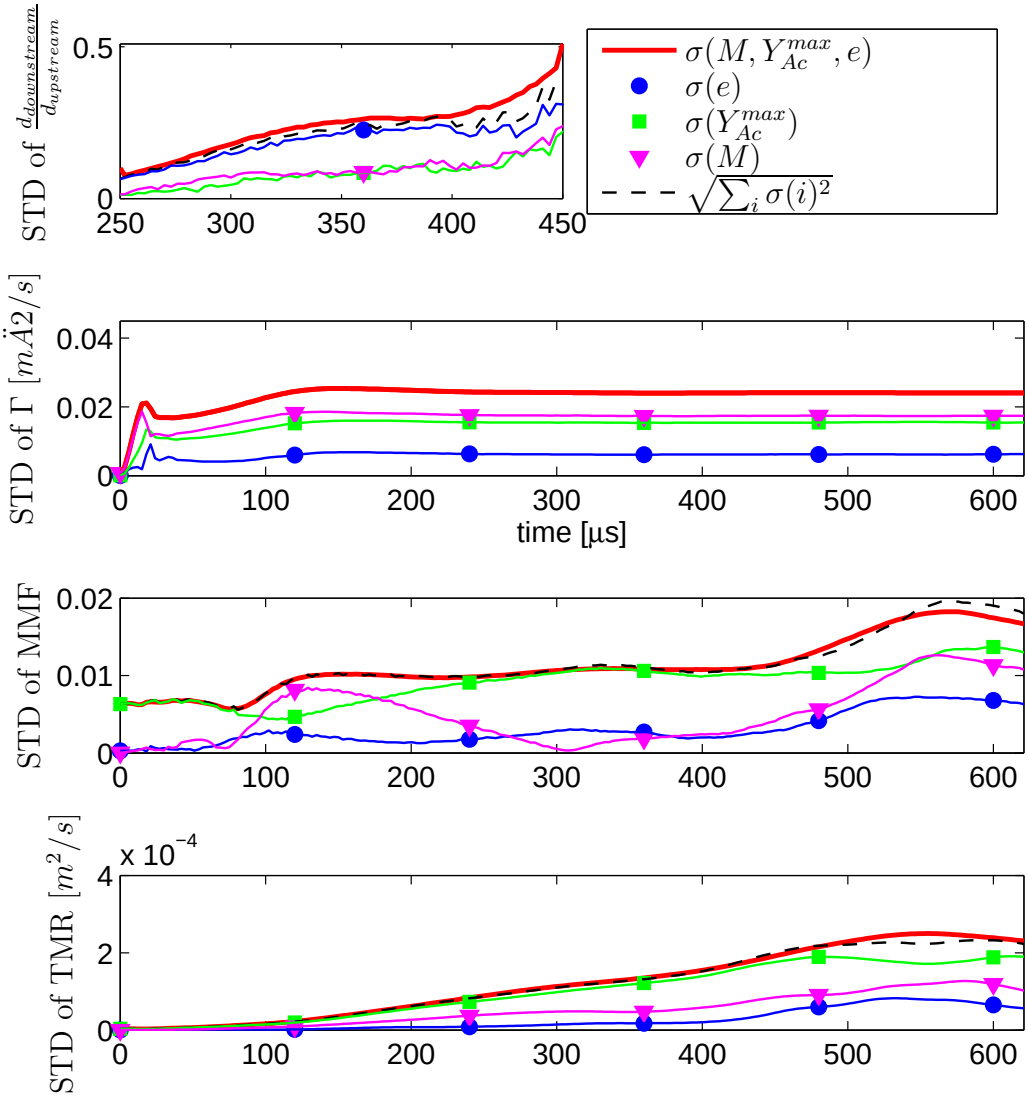

Figure 5.9.: Standard deviations of single uncertain parameter variations and multiple parameter variation.

these figures show the multivariate standard deviation $\sigma(e, M, Y_{Ac}^{max})$ and $\sqrt{\sum_i \sigma(i)^2}$. The latter is the exact multivariate standard deviation for uncorrelated random variables characterized by vanishing covariance. The weak correlation of the three uncertainty parameters is reflected by the fact $\sqrt{\sum_i \sigma(i)^2} \approx \sigma(e, M, Y_{Ac}^{max})$ during the entire simulation time $0\ \mu s \leq t \leq 640\ \mu s$.

Standard deviation of characteristic points of the bubble $x_{upstream}$, $x_{centroid}$ and $x_{downstream}$ is totally dominated by variation of the Mach number, i.e. $\sigma(e, M, Y_{Ac}^{max}) \approx \sigma(M)$. Variation of e and Y_{Ac}^{max} almost does not affect STD. Shankar et al. in [2] have also stated that the centroid location is insensitive to the initial acetone concentration.

STD of l_x and l_y is mostly affected by variation of eccentricity in the beginning, since e defines the initial l_x and l_y. At later times the impact of e on STD of l_x becomes weaker, whereas the influence of M and Y_{Ac}^{max} becomes stronger. STD of l_y at late times is equally affected by all three uncertain parameters.

It is possible to identify most important sources of variation of $\frac{d_{downstream}}{d_{upstream}}$ only for the simulation time between 250 μs and 450 μs, since the curves are smooth only in this time interval. It seems that e has greater importance than M and Y_{Ac}^{max}.

STD of Γ is equally influenced by M and Y_{Ac}^{max}, whereas e has minor importance. The baroclinic vorticity production $\frac{D\omega}{Dt} = \frac{1}{\rho^2}(\nabla\rho \times \nabla p)$ is the most important source of vorticity deposition in the case of SBI [15]. M and Y_{Ac}^{max} have direct influence on $|\nabla p|$ and $|\nabla\rho|$. The eccentricity changes the misalignment of ∇p and $\nabla\rho$ but this effect is not strong enough in comparison to the impact of the two other uncertainty parameters.

STD of TMR is mostly affected by Y_{Ac}^{max}, since it changes ∇Y_{Ac} which is involved in computation of TMR (see Eq. (3.6.5)). For the same reason Y_{Ac}^{max} is the most important parameter for variation of MMF.

5.2.3. Local Sensitivities

Local sensitivities for each output parameter (response function R_i) $\frac{\partial R_i}{\partial \xi_j}$, evaluated at uncertain variable means $\langle \xi_j \rangle$ are shown in Fig. 5.10 and 5.11. Interpretation of $\frac{\partial R_i}{\partial \xi_j}$ should be done with caution, since it is a local quantity, not like σ which describes global system behavior. It gives only the derivative at the mean value, i.e. it tells which tendency (increasing or decreasing) has the output parameter if the uncertain parameter is slightly changed. To avoid different dimensions of the derivatives, e, M and Y_{Ac}^{max} are written dimensionless as standardized random variables.

Increasing of M from the mean value causes increasing of $x_{upstream}$, $x_{centroid}$ and

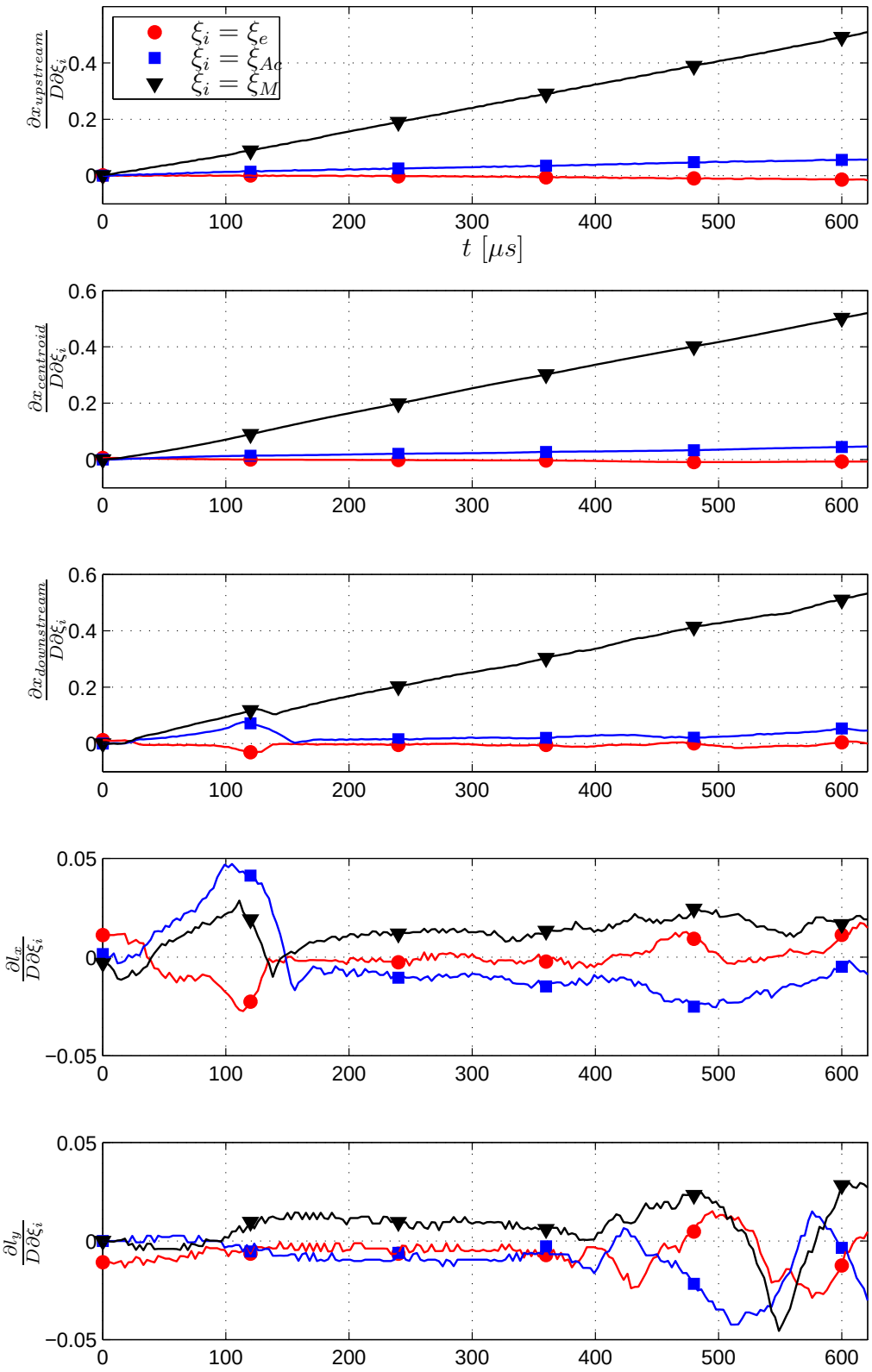

Figure 5.10.: Local sensitivities.

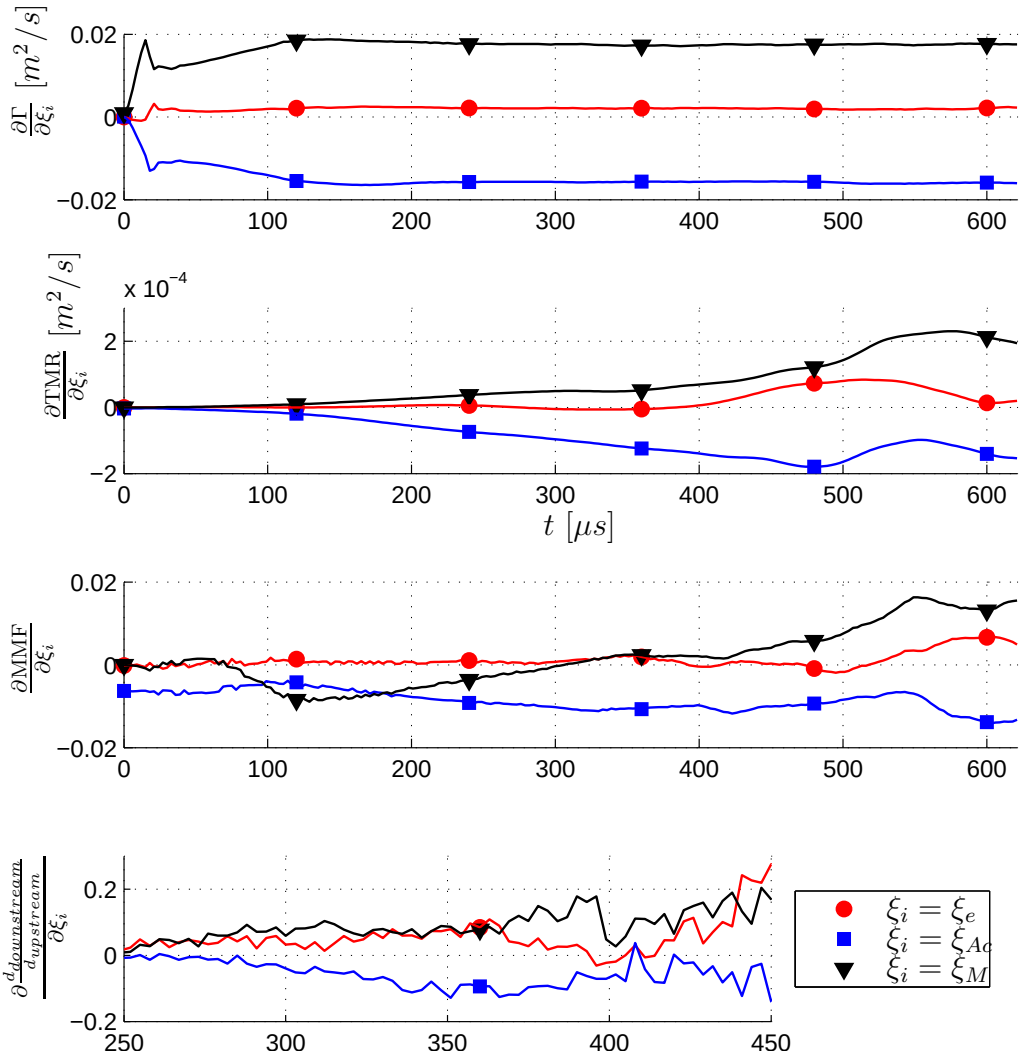

Figure 5.11.: Local sensitivities.

$x_{downstream}$, whereas increasing of e and Y_{Ac}^{max} does not considerably change location of the characteristic points.

It is remarkable that the derivatives $\frac{\partial l_y}{D\partial\xi_i}$ and $\frac{\partial l_x}{D\partial\xi_i}$ change the sigh through the simulation, i.e. at one instance the uncertain parameter ξ_i causes growing of the output parameter and at another instance if effects decreasing of the output parameter.

Higher Mach number increases Γ, since $\nabla p \propto M$, and higher acetone concentration decreases Γ, since $\nabla\rho \propto \frac{1}{Y_{Ac}^{max}}$ (see Fig. 3.5). Stretching the bubble in the streamwise direction slightly contributes to growing of Γ.

TMR grows with increasing M, i.e. the mixing process is enhanced with increasing M. TMR falls with growing acetone concentration, since $\nabla Y_{SF_6} \propto \frac{1}{Y_{Ac}^{max}}$ (see Fig. 3.4). Change of the bubble shape affects TMR only at late times. TMR is slightly growing with increasing of the eccentricity.

MMF decreases with increasing acetone concentration, since $Y_{SF_6} \propto \frac{1}{Y_{Ac}^{max}}$ (see Fig. 3.4). The effect of the Mach number drastically changes in time. At early times MMF decreases with increasing M and at late times MMF does the opposite.

In the smooth area of $\frac{\partial \frac{d_{downstream}}{d_{upstream}}}{\partial\xi_i}$ the derivative at the mean value is close to zero. It might indicate that maximum or minimum of $\frac{d_{downstream}}{d_{upstream}}$ is located close to its mean value. Nevertheless if the derivative at the mean value is zero, it does not mean there is no variation in $\frac{d_{downstream}}{d_{upstream}}$. The ratio of spiral widths varies according to Fig. 5.5 and 5.7.

6. Conclusion

In the present study the attempt was made to identify the uncertainty parameters in the shock interaction with a heavy gas bubble.

It was found that the relative deviations of the geometrical quantities and of the circulation are smaller than the relative deviations of TMR and MMF.

The Mach number has the strongest impact on the position of characteristic points of the bubble. The variation of TMR and MMF are mostly affected by the variation of the bubble contamination with acetone. The deviation of the circulation is equally strong influenced by the Mach number and the contamination with acetone. Whereas the size of the mixing area depends on all three uncertainty parameters.

The local variation of the output quantities of interest is not obvious in general. The variation of an uncertain parameter can lead to growing of an output quantity at one time and to decreasing at another time.

To reproduce the experiment numerically it is of paramount importance to know the initial Mach number and the heavy gas concentration from the experiment, i.e. these quantities should be measured as precise as possible. It is difficult to measure and to model a certain deformation, therefore the shape of the heavy gas cylinder should be kept as close as possible to a circle.

This study could not reflect all aspects of SBI because of the complexity of the problem. There are several possible extensions to this work:

1. Performing simulations on finer grid.
2. Simulation of the entire bubble in two dimensions. That allows unsymmetrical deformation of the bubble.
3. Higher order uncertainty quantification
4. Extension to three dimensional simulation to account for three dimensional effects.

Bibliography

[1] C. Tomkins, S. Kumar, G. Orlicz, and K. Prestridge. An experimental investigation of mixing mechanisms in shock-accelerated flow. *J. Fluid Mech.*, 611:131, 2008.

[2] S. K. Shankar, S. Kawai, and S. K. Lele. Two-dimensional viscous flow simulation of a shock accelerated heavy gas cylinder. *Phys. Fluids*, 23(2):024102, 2011.

[3] X. Y. Hu, Q. Wang, and N. A. Adams. An adaptive central-upwind weighted essentially non-oscillatory scheme. *J. Comput. Phys.*, 229(23):8952, 2010.

[4] R. D. Richtmyer. Taylor instability in shock acceleration of compressible fluids. *Communications on pure and applied mathematics*, XIII:297, 1960.

[5] E. E. Meshkov. Instability of the interface of two gases accelerated by a shock wave. *Fluid Dyn.*, 4(101), 1969.

[6] B. D. Collins and J. W. Jacobs. PLIF flow visualization and measurements of the Richtmyer–Meshkov instability of an air/SF6 interface. *J. Fluid Mech.*, 464:113–136, 2002.

[7] S. K. Shankar, S. Kawai, and S. K. Lele. Numerical Simulation of Multicomponent Shock Accelerated Flows and Mixing using Localized Artificial Diffusivity Method. (January), 2010.

[8] S. Balasubramanian, G.C. Orlicz, and K.P. Prestridge. Experimental study of initial condition dependence on turbulent mixing in shock-accelerated richtmyer-meshkov fluid layers. *Journal of Turbulence*, 00(00), 2011.

[9] A. W. Cook. Enthalpy diffusion in multicomponent flows. *Phys. Fluids*, 21:055109, 2009.

[10] S. Chapman and T. G. Cowling. *The Mathematical Theory of Non- Uniform Gases: An Account of the Kinetic Theory of Viscosity*. Cambridge University Press, 1990.

[11] R. C. Reid, J. M. Pransuitz, and B. E. Poling. *The Properties of Gases and Liquids*. McGraw Hill, 1987.

[12] J. D. Ramshaw. Self-consistent effective binary diffusion in multicomponent gas mixtures. *J. Non-Equilib. Thermodyn.*, 15(295), 1990.

[13] J. D. Anderson. *Modern Compressible Flow with Historical Perspective, 2nd edition.* McGraw Hill, 1990.

[14] B. M. Adams, K. R. Dalbey, M. S. Eldred, L. P. Swiler, W. J. Bohnhoff, J. P. Eddy, D. M. Vigil, P. D. Hough, and S. Lefantzi. DAKOTA, A Multilevel Parallel Object-Oriented Framework for Design Optimization, Parameter Estimation, Uncertainty Quantification, and Sensitivity Analysis. Version 5.2 Theory Manual.

[15] D. Ranjan, J. Oakley, and R. Bonazza. Shock-Bubble Interactions. *Annu. Rev. Fluid Mech.*, 43(1):117–140, 2011.

A. Appendix

A.1. extractInput.F90

This program extracts values of uncertainty parameters defined by Dakota for uncertainty analysis. It has to be chosen as analysis driver in "dakota.in" file (see example of dakota.in in A.3).

```
!FTN95 application
PROGRAM main
IMPLICIT NONE
INTEGER :: inputNo, outputNo, i
!single precision:
integer, parameter :: sp = selected_real_kind(6, 37)
!double precision:
integer, parameter :: dp = selected_real_kind(15, 307)
!quad precision:
integer, parameter :: qp = selected_real_kind(33, 4931)

!dynamic memory allocation for input and output values real(kind=dp),
!dimension(:), allocatable :: inputVector
real(kind=dp), dimension(:), allocatable :: outputVector

!Every time Dakota needs response function values at
!certain values input parameters, it creates file
!"params.in", where values of the input parameters are
!stored, and a file 'results.out', where required
!response function values are taken from.

OPEN(unit=23, file='params.in')
!the first variable in the file is the number of input variables.
READ(23,*) inputNo
!Fortran will automatically advance cursor without
!reading next variable on line
allocate (inputVector(inputNo)); inputVector=0;

!read values of input parameters
do i = 1, inputNo
        READ(23,*) inputVector(i);
      end do

!read number of output variables
READ(23,*) outputNo;
```

```
CLOSE(23);
allocate (outputVector(outputNo)); outputVector=0;

!Since the aim of the this program is to extract the
!input values, the response function values are not
!important and can be set to an arbitrary value,
!e.g. to 1.
OPEN(unit=24, file='results.out')
do i = 1, outputNo
      WRITE(24,*) 1, "␣f"
      end do
CLOSE(24);

!create file "inputDataStructured", values for each
!input parameter are stored in differnet columns.
open(unit=25, file='inputDataStructured', POSITION='APPEND')
WRITE(25,'(3en)',advance='NO') inputVector(1:inputNo);

!create file "inputData" with all values for all input
!parameters in one column.
open(unit=25, file='inputData', POSITION='APPEND')
WRITE(25,'(en)',advance='yes') inputVector(1:inputNo);
END PROGRAM
```

A.2. insertOutput.F90

This program delivers response function values which belong to to input parameters values denifed by Dakota for uncertainty analysis. It has to be chosen as analysis driver in "dakota.in" file (see example of dakota.in in A.3).

```
!FTN95 application...
PROGRAM main
IMPLICIT NONE
INTEGER :: inputNo, inputNo1, outputNo, outputNo1, i, j, stepsNo, k, l
!single precision:
integer, parameter :: sp = selected_real_kind(6, 37)
!double precision:
integer, parameter :: dp = selected_real_kind(15, 307)
!quad precision:
integer, parameter :: qp = selected_real_kind(33, 4931)

real(kind=dp), dimension(:), allocatable :: inputVector
real(kind=dp), dimension(:), allocatable :: outputVector
!specify input/output dimensions, number of simulation steps
outputNo=11; inputNo=3; stepsNo=125;
type entry
        real(kind=dp), dimension(inputNo) :: input
        real(kind=dp), dimension(outputNo) :: output
end type entry
type(entry), dimension(:), allocatable :: vectorData
```

```
!dynamic memory allocation for input parameters
allocate (vectorData(stepsNo));

!read manually created file 'dataForDakota' with input
!quantities and corresponding response function values.
! All data have to be in one column.
OPEN(unit=24, file='dataForDakota')
do j=1, sampleNo
        do i=1, inputNo
          READ(24,'(en)', end=999)
          vectorData(j)%input(i);
          vectorData(j)%input(i)=ANINT(vectorData(j)%input(i)*1e4)*1e-4;
        enddo
        do i=1, outputNo
                READ(24,'(en)', end=999) vectorData(j)%output(i);
        enddo
enddo
999 continue
CLOSE(24)

!read the file "params.in" which is created by Dakota.
OPEN(unit=23, file='params.in')
READ(23,*) inputNo1
!Fortran will automatically advance cursor without
!reading next var on line
allocate (inputVector(inputNo)); inputVector=0;
do i = 1, inputNo
         READ(23,*) inputVector(i);
        inputVector(i)= ANINT(inputVector(i)*1e4)*1e-4;
      end do
READ(23,*) outputNo1;
allocate (outputVector(outputNo)); outputVector=-7;
CLOSE(23);

!search for response function values which correspond to
!values of input parameters from "params.in" file.
do j=1, stepsNo
if ((vectorData(j)%input(1).eq.inputVector(1))
 & .and.(vectorData(j)%input(2).eq.inputVector(2))
 & .and.(vectorData(j)%input(3).eq.inputVector(3)) ) then
do l=1, outputNo
outputVector(l)=vectorData(j)%output(l)
end do
goto 998
else
k=1
endif
enddo
998 continue

!create file "results.out" with  response function
!values which are requested by Dakota.
```

```
OPEN(unit=25, file='results.out')
do i = 1, outputNo
      WRITE(25,*) outputVector(i), "␣f"
      end do
CLOSE(25);
END PROGRAM
```

A.3. dakota.in

This is an example of dakota.in, which can was used for uncertainty analysis.

```
strategy,
        single_method #graphics
        tabular_graphics_data

method,
        polynomial_chaos
        quadrature_order   5 5 5
        non_nested

variables,
        uniform_uncertain = 3
          lower_bounds   =-1.732050807568877-1.732050807568877 -1.732050807568877
          upper_bounds     =  1.732050807568877 1.732050807568877 1.732050807568877
          descriptors      = 'ECCENTRICITY' 'AcMassFraction' 'MachNumber'

interface,
        system
        analysis_driver = 'extractInput' #or 'insertOutput'
        parameters_file = 'params.in'
        results_file    = 'results.out'

responses,
        num_response_functions = 11
        no_gradients
        no_hessians
```